IMPLANTATION OF Ti INTO OXIDES FOR OPTICAL APPLICATIONS

A Thesis Presented to the

School of Graduate Studies

Addis Ababa University

In Partial Fulfilment

of the Requirement for the Degree

of Master of Science in Physics

By

Petros Thomas

June, 1995

ACKNOWLEDGEMENT

I am extremely grateful to Dr. S. Mantl who has enabled me to join the research group at the Institute of Thin Film and Ion Technology- 2 (ISI-2), KFA- Juelich, Germany. I am also greatly indebted to my advisor Dr. Ch. Buchal for his constant assistance, invaluable guidance and friendly encouragement without any reservation during the whole period of my research work at the institute.

I would like to express my due thanks to all members of the ISI-2 group for their unreserved assistance while I was carrying out my experiments. I am particularly grateful to L. Beckers and S. Bauer for their encouragement and continued follow up of the experimental work. Also, many thanks to Drs. M. Fleuster and K. Radermacher whose valuable suggestions, useful advises accounted a lot in dealing my research.

It is my pleasure to express my heartfelt gratitude to my advisor and instructor Dr. U. Stutenbaumer, Addis Ababa University, for his helpful suggestions and comments.

I would like to extend my appreciation to the Deutscher Akademischer Austauschdienst (German Academic Exchange Service) DAAD- for the financial support I received during my M.Sc. study, without which the study would not have been possible. My thanks are also due to Dr. F. Dworschak who spent his precious time looking for a qualified and appropriate advisor.

Abstract

Titanium (Ti^{+2}) implantation and annealing of lithium niobate ($LiNbO_3$) and sapphire (Al_2O_3) has been investigated using RBS and SIMS measurements. The implantation was done at room temperature with doses- $10^{15}Ti/cm^2$, $10^{16}Ti/cm^2$, $5x10^{16}Ti/cm^2$ and $10^{17}Ti/cm^2$. The energy of implantation was 400 keV. After implantation the samples were annealed with oven (1060^0C for one hour) and rapid thermal annealer (1060^0C for one minute). For the Al_2O_3 samples high temperature furnace annealing (1400^0C for one hour) was also used. Then, the implanted and annealed samples were analysed with Rutherford Backscattering Spectrometry using He^+ ions as the analysing beam with an energy of 1.4 MeV. Moreover, the $LiNbO_3$ samples were analysed with Secondary Ion Mass Spectrometry. The paper presents the experimental results obtained from the RBS and SIMS measurements.

CONTENTS

1. INTRODUCTION

The development of ion implantation as a technique for the surface modification of materials has traditionally focused on metals and semiconductors. This is primarily because implantation techniques have found most of their technological applications within these two classes of materials. For example, ion implantation plays an essential role in the electrical doping of devices, and the capabilities and versatility of implantation techniques have helped drive the explosive growth in this area. In the case of metals, ion implantation has found a technological niche and proved extremely useful in rendering surfaces harder, less corrosive, and with better wear properties.

The future for ion implantation techniques will certainly expand beyond semiconductors and metals. New uses of this technology are developing, and one promising field is that of optical materials. The use of ion implantation to change the physical properties, mainly the optical quality of optoelectronic materials has become important because it is applicable to produce integrated optical devices as waveguides, couplers, modulators, switches, light sources, detectors, and also more complex structures.

In contrast to other techniques for the modification of surface layers (diffusion, epitaxy, layer deposition, ion exchange), ion implantation has the advantage of achieving a reproducible and homogeneous change of the optical parameters in a very well defined volume region and the nature of the process is inherently nonequilibrium. Ions are usually implanted with energies far exceeding the thermal energy of the atoms of the target. In addition, the time required to distribute the excess energy among the atoms involved in the collision is short (typically picoseconds), resulting in effective quench rates in excess of millions of ^{o}K per second [1]. Hence, an asset of this technique is the ability to modify

thin layer on the surface and diffusing it into the substrate at high temperatures. The usefulness of thermal diffusion to introduce dopants, however, is limited by several characteristics of the diffusive process.

The use of ion implantation to introduce the dopants has been shown to result in several advantages: notably, a high concentration of dopant, steep concentration gradient at the edges of the guides, and short annealing times. Even though, the implantation produces large amounts of damage in the crystal lattice, forcing the near surface of the substrate into the amorphous state to a depth equal to the range of the deepest implanted ions, the doped material can be epitaxially regrown and stoichiometry can be restored by annealing the substrate in an oxygen atmosphere at high temperatures.

Ch. Buchal et al [3] reported for the first time the possibility of fabricating high-quality optical waveguides in $LiNbO_3$ by Ti implantation. After implantation they annealed the samples with oven at 1000^0C for one hour and found out that the implanted and annealed samples contain much more Ti and are much narrower than the conventionally indiffused samples.

However, Ti implantation followed by rapid thermal annealing of $LiNbO_3$ has not been reported up to now. Hence, we performed Ti implantation on $LiNbO_3$ with different doses and annealed the samples with rapid thermal annealer (RTA) and compared the results with that of the oven annealing.

Several attempts to implant Ti into Al_2O_3 for the fabrication of a Ti:sapphire waveguide laser have failed, since a sufficient epitaxial regrowth of the sapphire could not be established. Hence, we also tried to investigate Ti implantation of sapphire followed by different annealing methods and conditions.

2. Crystallographic Structures

2.1. Introduction

A very attractive combination of piezoelectric and optical properties has made lithium niobate one of the most extensively studied materials in recent years. Lithium ni (LiNbO$_3$) is centrally important in integrated and guided wave optics. It is a human-made dielectric material that does not exist in nature. It is now one of the most widely used electro-optic materials. This ferroelectric material has a trigonal crystal structure and is characterized by large pyroelectric, piezoelectric, electro-optic, and photoelastic coefficients. Lithium niobate is naturally birefringent. It has useful acoustic wave properties and a relatively large acousto-optic figure-of-merit. In addition it exhibits a very strong bulk photovoltaic effect. This effect causes efficient charge migration within the material and in combination with the material's linear electro-optic effect, it can produce a significant photorefractive effect (optically induced refractive-index changes).

This richness of large-magnitude physical effects has caused lithium niobate to become widely used in applications such as acoustic wave transducers, acoustic delay lines, acoustic filters, optical amplitude modulators, optical phase modulators, second harmonic generators, Q-switches, beam deflectors, phase conjugaters, dielectric waveguides, memory elements, holographic data processing devices, and others. It is clear that the detailed crystalline order is responsible for the usefulness of all these applications.

Lithium niobate is not completely characterized by the formula LiNbO$_3$. There are fairly large deviations from this stoichiometric composition. Most commercially available crystals have a composition that is significantly niobium-rich. The phase diagram of lithium niobate, given by Svaasand [4], is shown in Fig. (2.1). The diagram shows that this crystal has a fairly large solid-solution range from 44 to 50 mole %, and tends to grow with

variable composition. The solid- solution range is large at temperatures above 900°C but seems to be very narrow at low temperatures. Since lithium niobate is grown from congruent melts it is inherently metastable at room temperature.

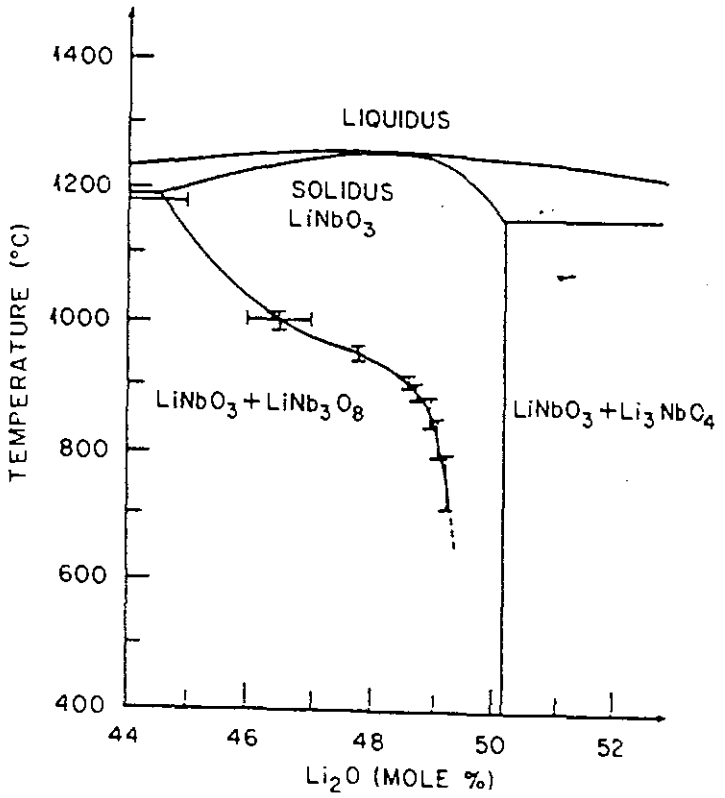

Fig. 2.1 Phase diagram in the existence regime of $LiNbO_3$ (Svaasand et al. [4]).

2.2. Crystal Structure of $LiNbO_3$

$LiNbO_3$ is a ferroelectric material with an unusually high Curie point (approximately 1420°C [2]). In the ferroelectric phase (for temperatures below the Curie point) a $LiNbO_3$ crystal exhibits three-fold rotational symmetry about its c-axis. Thus it is a member of the trigonal crystal system. In the trigonal system, two quite different unit cells can be chosen: hexagonal or rhombohedral. The conventional hexagonal unit cell in $LiNbO_3$ contains six formula weights while the conventional rhombohedral contains two formula units. The measured unit cell parameters for the two choices of axes is shown in Table I [5].

Table I

Unit Cell Parameters of $LiNbO_3$ in the Ferroelectric Phase

Parameters for hexagonal axes

$a_H = 5.150 \pm 0.002\ A^0$
$c_H = 13.867 \pm 0.005\ A^0$

number of formula units: 6 per unit cell

Parameters for rhombohedral axes

$a_R = 5.496 \pm 0.002\ A^0$
$\alpha_R = 55.87^0 \pm 0.02$

number of formula units : 2 per unit cell

In the high-temperature phase (for temperatures above the Curie point) $LiNbO_3$ loses its polar axis. The basic net of both structures, the ferroelectric phase and the high temperature phase, is formed by six equidistant plane layers of oxygen per unit distance, stacked in the direction of the triad axis. The origin of the coordinate system has to be chosen on the triads for both structures. In the high temperature phase, it is fixed in the center of an oxygen octahedron, midway between two oxygen layers, and is occupied by a niobium ion. In the ferroelectric phase, the z-position of the origin can be arbitrarily chosen. It seems to be more convenient to leave the origin midway between two oxygen layers, in the vicinity of a niobium ion. The z-coordinates of the oxygen layers become $\frac{1}{12}, \frac{3}{12}, \frac{5}{12}, \frac{7}{12}, \frac{9}{12}$, and $\frac{11}{12}$. It is useful then to divide the c- axis of the unit cell in twelve equal parts, and to give all Z parameters of Li and Nb as deviations from these idealized positions. The oxygen arrangement can be described by a distorted hexagonal close packing. The peculiarities of the $LiNbO_3$ structure arise from the very special arrangement of the cations. Let us start with the discussion of the high temperature phase. Although the measurements of the position of Nb and Li in this structure are not very precise, plausible assumptions can be made. The stacking of the cations can be easily visualized by looking at an atomic row with coordinates (0,0,c) a c-row. Fig. 2.2 shows the main features. The

c-axis has been divided into 12 parts, all c-coordinates now being given in twelfth of c. Oxygen layers are then at 1,3,5,7,9, and 11. There are alternating cations (Fig. 2.2 a) at

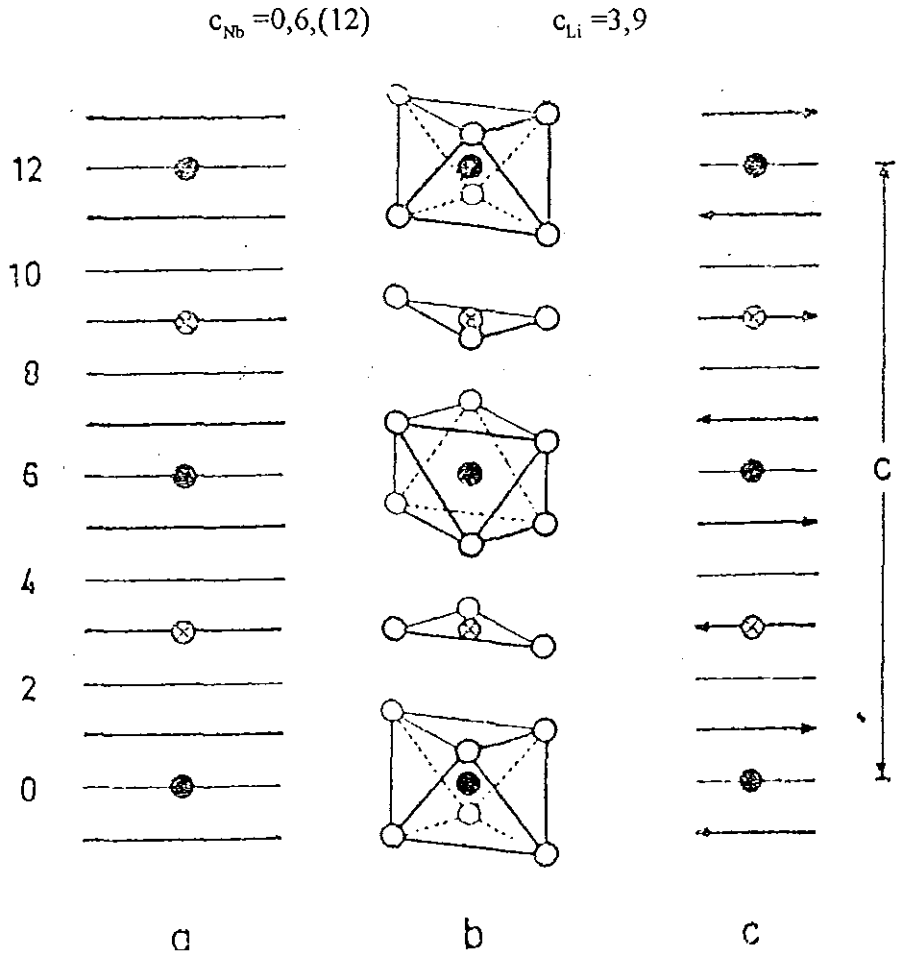

Fig. 2.2 Stacking sequence of cations in $LiNbO_3$. (a) Heavy lines denote oxygen layers. (b) Oxygen environment of cations (slightly idealized). (c) Same as (a), but arrows indicating directional sense of oxygen triangles [5].

The nearest oxygen neighbors of the cations are arranged in triangles (Fig. 2.2 b). The niobium ions are surrounded by two triangles at -1 and +1, thus forming an octahedron. The Li ions are in the center of an oxygen triangle, the next nearest oxygen ions having a much larger distance. As can be seen from Fig. 2.2 (b) the oxygen triangles, forming a nearly hexagonal close packed structure, are alternatingly rotated about 180^0. If the direction sense of the triangle is indicated by an arrow, we obtain Fig. 2.2 (c). This figure clearly shows that the lattice is not repeated from Nb_0 to Nb_6 but to Nb_{12} if the oxygen environment is taken into account. The low temperature phase is characterized by a

fairly large displacement of both Li and Nb in the c-direction. This is sketched in Fig. 2.3. This figure also includes the directions of the piezoelectric +z and -z axes of the two domains.

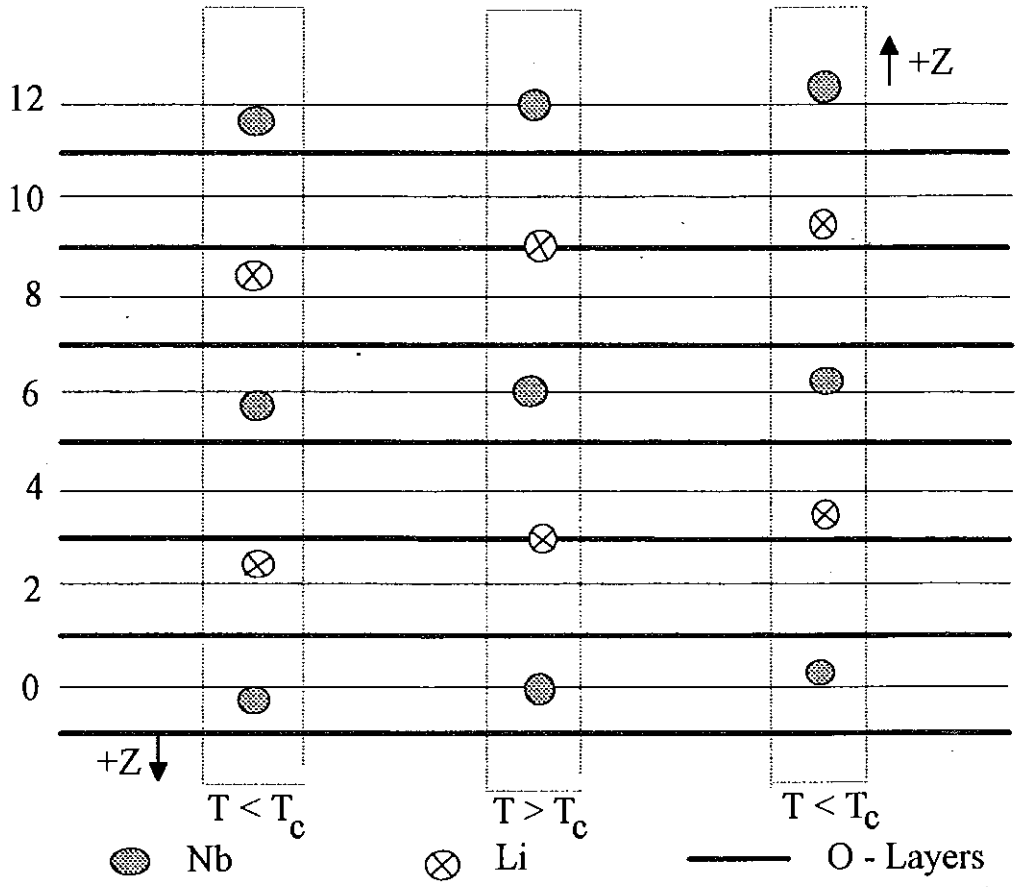

Fig. 2.3 Displacement of cations due to the ferroelectric phase transition for the two possible domain of direction [5].

Due to its displacement out of the oxygen layer the Li ion has a distorted octahedral environment in the low-temperature phase. This leaves another octahedral site vacant. The stacking order of octahedral sites in a c-row becomes:

... Nb - Vac. - Li - Nb - Vac. - Li - Nb - Vac. ..

The distortive movement of the oxygen ions in their respective planes is small and may be neglected in first order. Nevertheless it is of much importance to the movement of the Li ion. At low temperatures the distortion of the oxygen lattice leads to a contraction of the triangular interstitial site occupied by Li at high temperatures. This forces the lithium

ion to one of the sites equidistant from the triangle above and below it. The potential well in the "window" formed by the three oxygen ions seems to be very high. This potential barrier must be surmounted during polarization reversal which seems to be nearly impossible at low temperatures.

2.3. Crystal Structure of Al_2O_3

Sapphire belongs to the ilmenite structure (rhombohedral), similar to $LiNbO_3$, with the large O^{2-} ions arranged in close-packed layers and filling the available volume nearly completely. The Al^{3+} cations find positions between O^{2-} layers, such that they are surrounded by six O^{2-} anions in an octahedral position as shown in Fig. 2.4[6]. The octahedron is not regular but is severely distorted along a threefold direction which coincides with the c axis of the crystal. 2/3 of the available octahedral sites are occupied, 1/3 remain vacant.

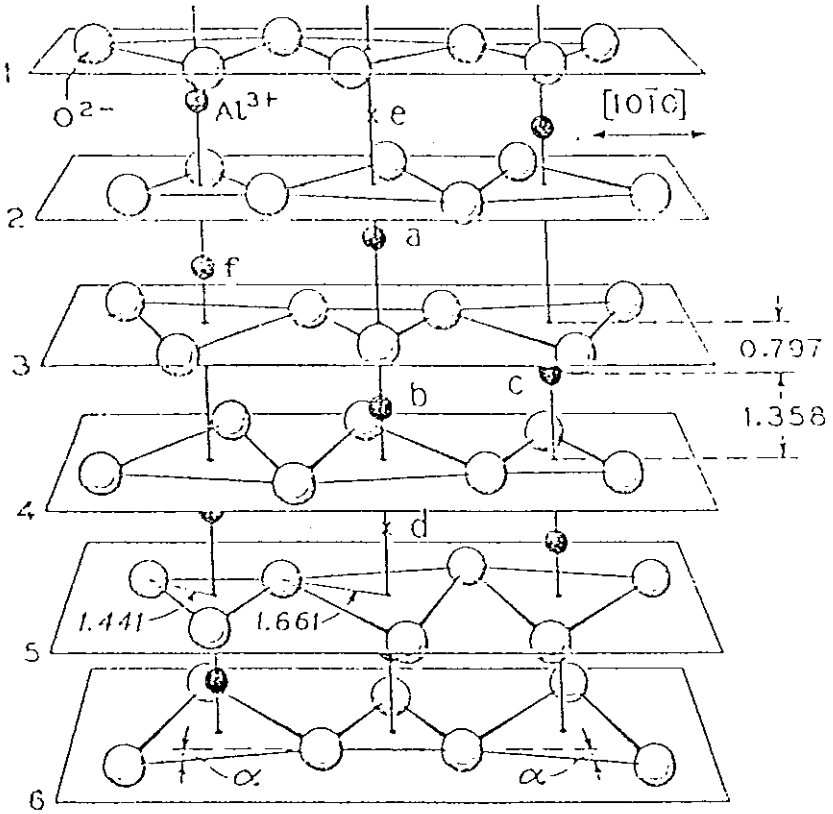

Fig. 2.4 Portion of the Al_2O_3 lattice. The Al ions are between equally spaced planes of oxygens. They are in octahedral oxygen coordination but the octahedron is severely distorted [6]

Along the hexagonal c-axis the Al- sublattice shows well ordered vacant octahedral sites which are structural vacancies:

... Al - Al - Vac. - Al - Al - Vac. ...

These structural vacancies are ordered to minimize the Coulomb energy and hence to maintain the electrostatic force in the crystal.

3. ION IMPLANTATION

3.1. Introduction

The process of ion implantation relies on the possibility of injecting energetic ions relatively deep into a solid. In achieving this deep penetration ions must interact and collide, individually or collectively, with atoms of the solid matrix. During these collisions, energy will be exchanged between the moving ion and the initially stationary lattice atoms with a concomitant energy loss by the ions and an energy gain by the atoms. The energy loss serves to slow down the ions, eventually to rest in the lattice; the atomic energy gain results in the creation of defects or disorder in the lattice. In addition to energy loss, the injected ion will suffer deflections at each separate or multiple collision encounter and the sequence of these deflections will determine its detailed trajectory in the solid. Similarly, the trajectories of lattice atoms which gain sufficient energy to be displaced from their normal positions will be dictated by their energy transfer and deflection sequences. Thus the overall pattern of lattice disorder will depend upon the individual collision events. Since the ion and atom collision events occur sequentially and are separable, the central problem in predicting ion penetration and lattice disorder is therefore one of understanding the dynamics of the collision between a moving ion and an initially stationary atom.

During the process of ion implantation, atoms or molecules are ionized, accelerated in an electrostatic field, and implanted into a solid. In this way, a great many combinations of ions and substrates are possible. The acceleration energy can be between a few thousand electron volts (keV) and several million electron volts (MeV). The penetration depth of the ions depends not only upon the energy, but also upon the mass of the ions and the atomic mass of the solid. Thus, for example, the average range of 10 keV phosphorus ions in silicon is about 14 nm; that of 1 MeV boron ions is about 1756 nm [7]. As a result of such

an ion bombardment, it is possible to alter nearly all properties of the surface layer of the solid.

According to its nature, the process of implantation is basically independent of chemical solubility limits, the temperature during implantation, and the concentration of the dopant at the surface of the substrate. The doping atoms introduced have a concentration profile which is generally described by a Gaussian distribution, with an average projected range R_p and a standard deviation ΔR_p.

3.2 Basic Concepts of Ion Implantation

In order to discuss and describe ion implantation it is necessary to consider the different concepts and events that contribute to the overall picture. Amongst these will be the following:

1. Binary Collision. Although ion implantation involves a beam of many ions interacting with a solid containing many atoms, the collision between one ion and one target atom is of basic importance. In many circumstances the problem of an ion entering a solid can be treated as a succession of binary collisions in which the ion interacts or collides with only one target atom at a time. Consequently, a study of the dynamics of binary collisions is essential in any study of ion implantation.

2. Interatomic Potential. The collision between two atoms depends intrinsically on the interatomic potential V(r). The forces acting on both particles and hence their trajectories are derived from V(r) so that a knowledge of the interatomic potential is of fundamental importance. We need therefore to discuss the different approaches employed to obtain satisfactory expression for V(r).

3. Energy Loss. As an ion penetrates a solid it loses its energy in a series of collisions with the target atoms until it eventually comes to rest. The amount of energy lost

in each collision will decide the total path length or range of the ion. Energy loss is considered to occur by either elastic or inelastic processes. In the former, kinetic energy is conserved and in the latter, is converted into another form by excitation of atomic electrons.

4. Ion Range. The range of an ion is determined by the rate at which it loses energy. Having described and evaluated energy loss processes we can calculate ion ranges and predict the spatial distribution of implanted impurities within surface layers of targets. In non-crystalline or amorphous materials, energetic implanted ions have a Gaussian- shaped distribution but in single crystals the picture becomes complicated because the crystal structure assumes a role in determining the range profile.

5. Channeling. In a single crystal the lattice atoms are arranged periodically in space in certain directions and the structure has open channels bounded by densely-packed walls. Ions entering in these directions often do not make a random sequence of collisions, as in an amorphous material, but rather are steered by a succession of correlated interactions with atoms in the channel walls.

6. Damage. Energy is transferred from the projectiles to the target atoms as they slow down. An atom receiving sufficient kinetic energy will be displaced from its lattice site and the target will suffer radiation damage. Since the energy required to displace an atom is typically ~25 eV [8], heavy ions with a few keV energies cause considerable damage. A recoiling target atom may itself be sufficiently energetic to act as a secondary projectile which in turn displaces further atoms and produces a cascade of displacement collisions.

7. Annealing. Atoms displaced during implantation may at a later stage return to their usual positions. This annealing may occur over a short time scale (e.g during the period that the collision cascades are moving through the lattice) or over much longer periods following completion of the implantation. The annealing is often assisted by

providing thermal energy. Radiation damage is often the inevitable outcome of ion implantation and may mask the desired doping effects. The mechanisms of radiation damage and annealing are consequently of vital importance.

8. Doping. The chemical and physical properties of most materials can be altered by the addition of impurities or dopants. These changes should be distinguished from those due to radiation damage. Doping by ion implantation should be compared and contrasted to other methods, principally that of thermally-activated diffusion. In this latter technique, the dopant is deposited on to the substrate surface and driven in by high temperature annealing, the dopant concentration profile being dependent on thermal equilibrium criteria for a particular dopant/ target combination. Ion implantation is a non-equilibrium process, the dopant atoms being driven into the solid by violent use of their excess kinetic energy. In this way compounds may be formed that are unattainable by other conventional methods.

3.3. Theoretical Background of Ion Implantation.

Basically, there are several different effects which occur during the bombardment of solids with heavy charged particles. However, the most dominant are

1. Inelastic collisions with bound electrons of the stopping medium. The energy loss in such collisions takes place by excitation or ionization of atoms or molecules.

2. Elastic collisions with nuclei or whole atoms, where by a part of the kinetic energy is transferred to the particles absorbing the impact.

Which of the two effects predominates depends upon the energy and the mass of the accelerated particles, as well as upon the mass and the atomic number of the medium. In the energy range important for ion implantation, both effects have to be considered. For the calculation of the stopping, one defines cross-sections for electronic and nuclear stopping, $S_{e,n}$, as follows

$$S_{e,n} = -\frac{1}{N}\left(\frac{dE}{dX}\right)_{e,n} \tag{3.1}$$

In figure 3.1, the general behavior of both stopping cross sections, dependent on the energy, is given [7]. The energies of ion implantation are lower than 1 MeV, Therefore, they are always in the region below E_3 . Beyond E_3 is the region where the theory of Bethe and Bloch is valid.

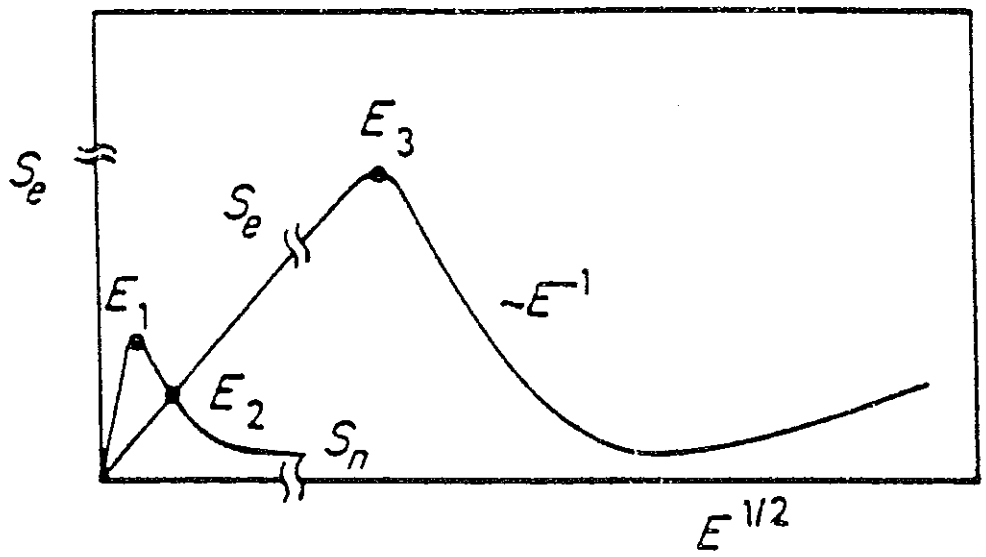

Fig. 3.1 Stopping power S_e and S_n as a function of energy (schematic) [7]

Only in recent years has there been any interest in the energy range of ion implantation; this was first theoretically investigated by Lindhard and Scharff [9]. According to this theory, the ions have a Gaussian range distribution around an averaged projected range R_p, with a standard deviation ΔR_p.

As has already been mentioned, two mechanisms for the loss of energy are to be considered at low energies; on the one hand, collisions of ions with free and bound electrons, and on the other, collisions with atomic nuclei. On the assumption that both processes are independent of each other, one obtains for the energy loss per unit distance

$$-\frac{dE}{dx} = N(S_n(E) + S_e(E)) \tag{3.2}$$

If $S_n(E)$ and $S_e(E)$ are known, it is possible to integrate equation (3.2)

$$N\int_0^R dx = -\int_E^0 \frac{dE}{S_n(E) + S_e(E)}$$

$$R = \frac{1}{N}\int_0^E \frac{dE}{S_n(E) + S_e(E)} \tag{3.3}$$

This gives the total path length for an ion slowing down from an energy E. R is the average range of a particle with the energy E in an amorphous medium.

3.3.1. Nuclear Stopping

The energy loss dE of an ion by elastic nuclear interaction in a layer dx is proportional to the atomic density N_n as well as to the total energy transferred in all individual collisions T_n, i.e.,

$$S_n(E) = -\frac{1}{N_n}\left(\frac{dE}{dx}\right)_n = \int_0^\infty T_n(E,p)2\pi p dp = \int_0^{T_m} T_n d\sigma(E, T_n) \tag{3.4}$$

where $d\sigma$ is the differential cross section ($d\sigma=2\pi pdp$) and p is the impact parameter, T_m is the maximum transferable energy for a central collision. Fig. 3.2. shows a typical scattering process between an ion and an atom. The incident ion is deflected by the angle θ_1, and transfers the energy T_n to the target atom, which leaves its original position at the angle θ_2. For values of p between ∞ and 0 one obtains values for $T_n(E,p)$ between 0 and T_m. T_m amounts to

$$T_m = \frac{4M_1M_2}{(M_1 + M_2)^2}E_0 \tag{3.5}$$

where M1 and M_2 are the masses of ion and target.

The calculation of $T_n(E,p)$ is a well known problem of classical mechanics

$$T_n(E,p) = E_0 \frac{2M_1M_2}{(M_1+M_2)^2}(1-\cos\Phi) \tag{3.6}$$

where Φ is the deflection angle in the center-of-mass system. When calculated according to Reference [10], the following expression for Φ is obtained

$$\Phi = \pi - 2p\int_0^{u_m} \frac{du}{(1-\frac{V(u)}{E_r}-p^2u^2)^{1/2}} \tag{3.7}$$

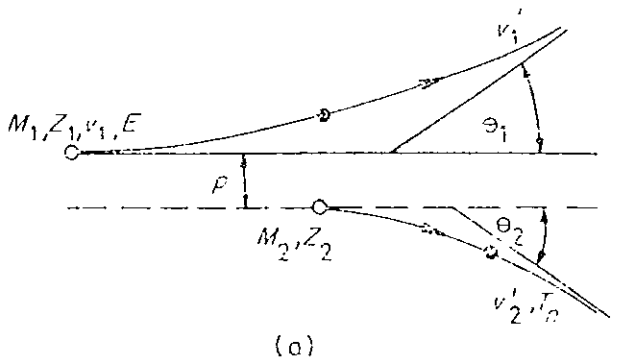

Fig. 3.2 Scattering between particles of mass M_1 and M_2, impact parameter p, scattering angle θ_1 and θ_2 [7]

Where u=1/r, $r = r_1+r_2$ is the distance between particles in the center- of- mass system, V(u) is the interaction potential, $E_r=E_0M_2/(M_1+M_2)$ is the energy of the ion in the center-of-mass system, and u_m is the reciprocal value of the minimum distance between the particles.

In order to solve equation (3.7), V(u) has to be known. If the screening effect of the electrons were to be neglected, the classical case of Rutherford for the scattering of α particles would be obtained, and V(u) could be directly written as the Coulomb potential.

For heavy particles of low velocity, and in the case of relatively distant collisions, the screening effect of the electrons cannot be neglected and the following is written

$$V(r) = \frac{Z_1 Z_2 q^2}{r} \varphi(r/a) \tag{3.8}$$

where φ(r/a) is a suitable screening function and a is the screening parameter (of the order of magnitude of the Bohr radius). Because of the use of the cgs system in the case of all the cited classical derivations, the factor $4\pi\varepsilon_0$ before r is missing in equation (3.8)

Analytical solutions can be given for power potentials (Lindhard and Scharff [9])

$$V(r) = \frac{Z_1 Z_2 q^2}{r} \frac{1}{s} \left(\frac{a}{r}\right)^{s-1} \tag{3.9}$$

However, the simple analytical form is lost for other values of s than 1 and 2. The approximation s=1 is realistic for collisions with high energy transfer, as is s=2 for collisions with low energy transfer (Lindhard and Scharff [9]). The best energy agreement with experimental results is obtained with the use of the statistical atomic model according to Thomas and Fermi [11], from which the screening function can be derived as a solution of the differential equation

$$\frac{d^2\varphi}{dx^2} = \varphi^{3/2}(x) x^{-1/2} \tag{3.10}$$

In this case a is obtained by

$$a = \frac{1}{2}\left(\frac{3}{4}\pi\right)^{2/3} a_0 \left(Z_1^{2/3} + Z_2^{2/3}\right)^{-1/2} \tag{3.11}$$

where a_0 is the Bohr radius ($a_0 \approx 0.053nm$). With use of this potential, Lindhard and Scharff calculated the effective differential cross-section for nuclear stopping. Using suitable normalization (reduction) for range and energy they obtained

$$\rho = C_R R = 4\pi a^2 N \frac{M_1 M_2}{(M_1 + M_2)^2} R \qquad (3.12)$$

$$\varepsilon = C_E E = \frac{a}{q^2} \frac{M_2}{Z_1 Z_2 (M_1 + M_2)} E$$

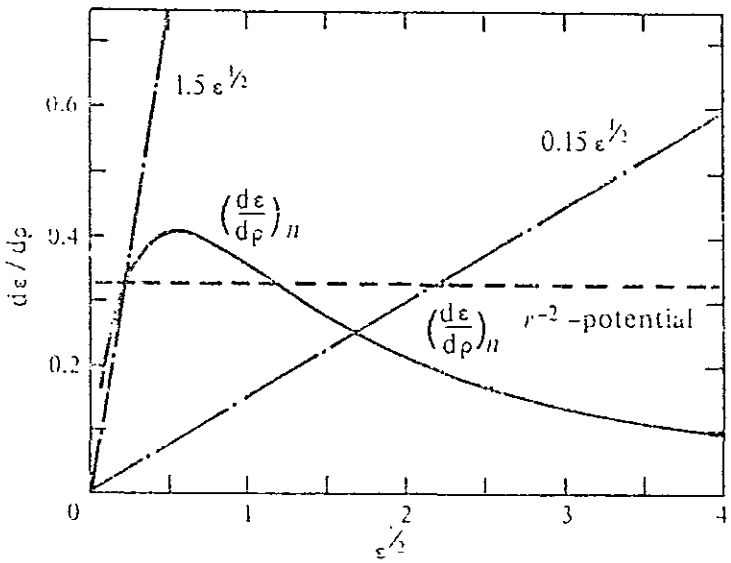

Fig. 3.3 Nuclear and electronic stopping powers in reduced units [8]

They succeeded in obtaining a generally valid dependence of the stopping power S_n upon the energy, for all ion-target combinations, which is dimensionless in the units used. A numerical calculation of the reduced stopping power is given Fig. 3.3, together with values for electronic stopping. The full drawn curve represents the Thomas-Fermi nuclear stopping power, the dot and dash lines the electronic stopping for k=0.15 and k=1.5. The dashed line gives the nuclear stopping power for the r^{-2} potential.

3.3.2. Electronic Stopping

Electronic stopping decreases with increasing particle velocity at high energies in the validity region of the Bethe theory, as shown in Fig. 3.1. The low-energy region was first investigated by Lindhard and Winter [12]. They assumed that the electrons form a free

electron gas and demonstrated that the electronic-stopping cross-section is proportional to the velocity of the ions, and therefore, proportional to the root of the energy

$$S_e(E) = -\frac{1}{N}\left(\frac{dE}{dx}\right)_e = k' E^{1/2}$$

$$\text{with} \qquad k' = \frac{kC_R}{C_E^{1/2} N} \tag{3.13}$$

$$\text{and} \qquad k = \xi_e \frac{0.0793\, Z_1^{1/2} Z_2^{1/2} (M_1 + M_2)^{3/2}}{\left(Z_1^{2/3} + Z_2^{2/3}\right)^{3/4} M_1^{3/2} M_2^{1/2}}$$

where ξ_e is a dimensionless constant of the magnitude $Z_1^{1/6}$; C_R and C_E are obtained from equation (3.12), and k is the proportionality constant in the normalized representation, i.e.,

$$-\left(\frac{d\varepsilon}{d\rho}\right)_e = k\varepsilon^{1/2} \tag{3.14}$$

The values for k are generally between 0.1 and 0.25.

A model has been developed by Firsov for the electronic stopping [13]. He assumed that the ion and the target atom, during the collision, form a quasi-molecule. This model has the advantage that it can be generalized to explain oscillations which occur in measured values of S_e [14]. In the case of amorphous media, the calculation is carried out similarly to that of the nuclear-stopping cross section.

One first calculates the energy loss, T_e , resulting from the electronic interaction between particles having the nuclear charges Z_1 and Z_2 , and then integrates over all impact parameters.

$$S_e = \int_0^\infty T_e(E,p) 2\pi p dp \tag{3.15}$$

As a specific example, if we implant $5x10^{19}$ ions/cm^2 of 40 keV boron into silicon then $R_p \sim 160$ nm and $\Delta R_p \sim 54$ nm so that from eq. (3.22), $N_p \sim 4 \times 10^{26}$ atoms/m^3.

3.5. Radiation Damage in Solids

In the preceding discussion, only the stopping of ions has been considered, without taking into account any effects upon the crystal lattice. Atoms can be displaced from their lattice sites, depending on the energy and the mass of the implanted ions as well as the mass of the target. The displaced atoms themselves can also displace other atoms, so that a collision cascade results. This leads to an accumulation of vacancies and interstitial atoms (Frenkel defects), as well as to complex lattice defects along the ion path (clusters). Heavy ions can transfer more energy to lattice atoms than lighter ones. A diagram showing formation of radiation damage is shown in Fig. 3.5 for light as well as heavy ions.

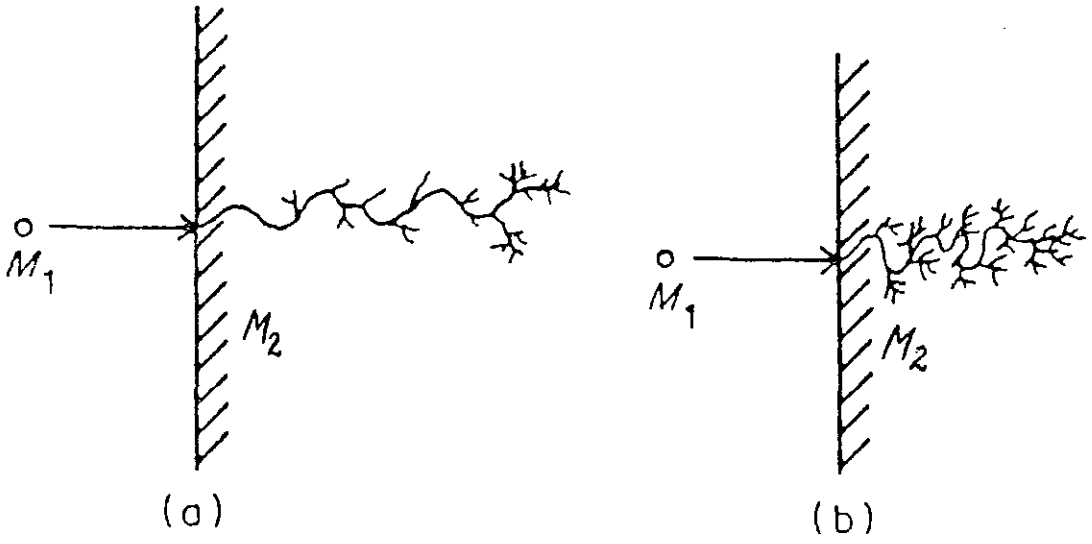

Fig. 3.5 Schematic representation of radiation damage formation:
(a) $M_1 < M_2$ (light ion); (b) $M_1 > M_2$ (heavy ion) [7]

The damaged areas begin to overlap with increasing dose, and finally form an amorphous layer extending to a certain depth, i.e., a layer in which there is no longer any long-range order in the lattice. The amount of radiation damage and its distribution depend on the ion species, the temperature, the energy and the dose.

4. Rutherford Backscattering Spectrometry

4.1. Concepts of a Backscattering Experiment and its Layout

The typical experimental system used today for routine backscattering analyses is shown in Fig. 4.1. It gives a schematic outline of the major components of such a system. Charged particles are generated in an ion source. Their energy is then raised to several MeV by an accelerator, usually a Van- de- Graaff (or a similar kind). The high-energy beam then passes through a series of devices which collimate or focus the beam and filter it for a selected type of particle and energy. The particles then enter the scattering chamber, are scattered by the target and impinges on the detector, where they generate an electrical signal. This signal is amplified and processed with fast analog and digital electronics. The final stage of the data has the form of a (digitalized) spectrum.

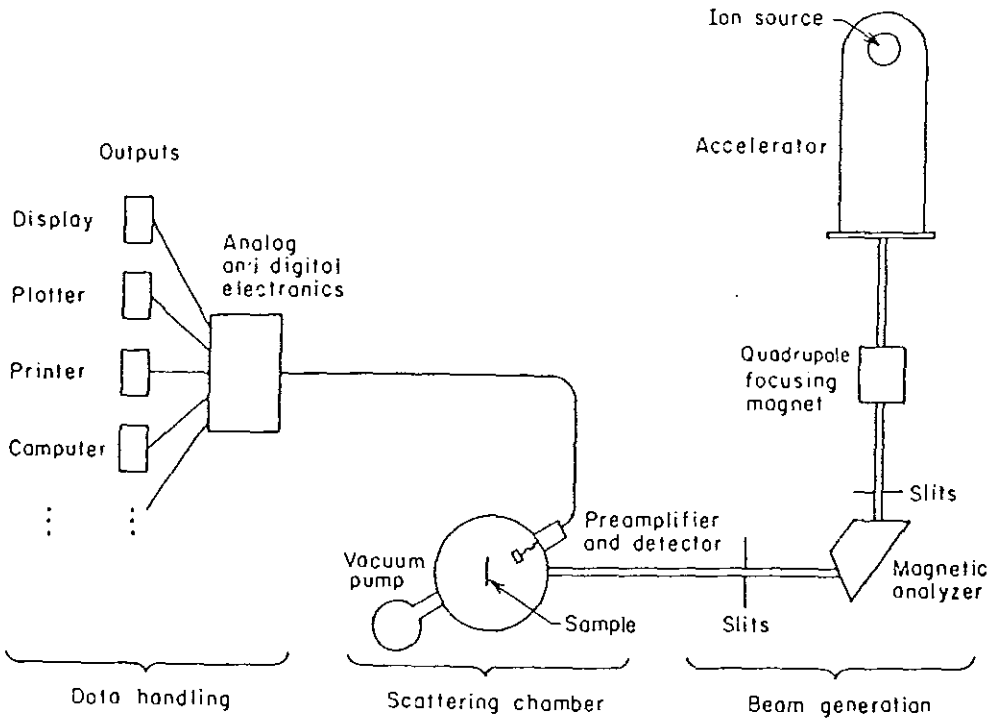

Fig. 4.1 Schematic diagram of a typical backscattering spectrometry system [15]

4.2. Basic Physical Processes

Only four basic physical concepts enter into backscattering spectrometry. Each one is at the origin of a particular capability or limitation of backscattering spectrometry and corresponds to a specific physical phenomenon. They are

1. Energy transfer from a projectile to a target nucleus in an elastic two-body collision. This process leads to the concept of the *kinematic factor* and to the capability of mass perception.

2. Likelihood of occurrence of such a two-body collision. This leads to the concept of *scattering cross section* and to the capability of quantitative analysis of atomic composition.

3. Average energy loss of an ion moving through a dense medium. This process leads to the concept of *stopping cross section* and to the capability of depth perception.

4. Statistical fluctuations in the energy loss of an ion moving through a dense medium. This process leads to the concept of *energy straggling* and to a limitation in the ultimate mass and depth resolution of backscattering spectrometry.

4.2.1. Kinematic Factor

When a particle of mass M_1, moving with constant velocity, collides elastically with a stationary particle of mass M_2, energy will be transferred from the moving to the stationary particle. In backscattering analysis, mass M_1 is that of the projectile atom in the analyzing beam and mass M_2 is that of an atom in the target examined. The assumption that the interaction between the two atoms is properly described by a simple elastic collision of two isolated particles rests on two conditions

(1) The projectile energy E_0 must be much larger than the binding energy of the atoms in the target. Chemical bonds are of the order of 10 eV, so that E_0 should be much larger than that.

(2) Nuclear reactions and resonance must be absent. This imposes an upper limit to the projectile energy. Nuclear processes depend on the specific choice of projectile and target atoms, so that the upper limit of E_0 varies with circumstances. With a H^+ beam, nuclear effects can appear even below 1 MeV; with He^+, they begin to appear at 2 to 3 MeV. [15]

The simple elastic collision of two masses M_1 and M_2 can be solved fully by applying the principles of conservation of energy and momentum. Let v_0 , v_0 and $E_0=1/2M_1v_0^2$ be the velocity, its value, and the energy of a projectile atom of mass M_1 before the collision, while the target atom of mass M_2 is at rest. After the collision, let v_1 and v_2 be the velocities and $E_1=1/2M_1v_1^2$ and $E_2=1/2M_2v_2^2$ be the energies of projectile and target atoms, respectively. The notation and the geometry of this scattering problem are given in Fig. 4.2, where the scattering angle θ and the recoil angle ϕ are defined as positive numbers with the arrows as shown. All quantities refer to a laboratory system of coordinates. Conservation of energy and conservation of momentum parallel and perpendicular to the direction of incidents are expressed by the equations

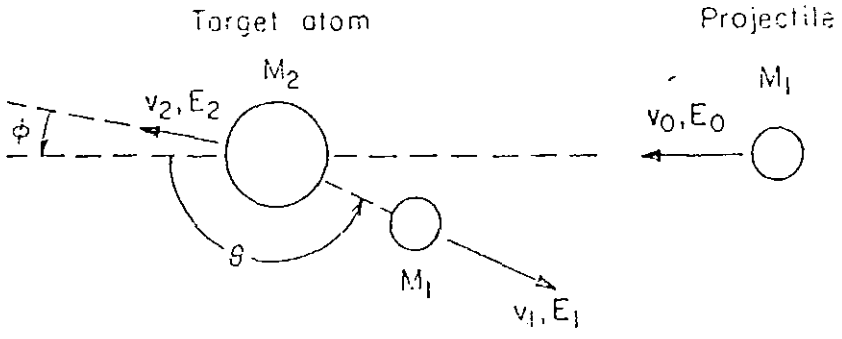

Fig. 4.2 Schematic representation of an elastic collision

$$M_1 v_0 = M_1 v_1 \cos\theta + M_2 v_2 \cos\phi \tag{4.1}$$

$$0 = M_1 v_1 \sin\theta - M_2 v_2 \sin\phi \tag{4.2}$$

Eliminating ϕ and v_2 , one finds

$$\frac{v_1}{v_2} = [\pm(M_2^2 - M_1^2\sin^2\theta)^{\frac{1}{2}} + M_1\cos\theta]/(M_2 + M_1) \tag{4.3}$$

For $M_1 \leq M_2$ the plus sign holds. We now define the ratio of the energy after the elastic collision to that before the collision as the *kinematic* factor K

$$K_{M_2} = \frac{E_1}{E_0} = \left[\frac{(M_2^2 - M_1^2\sin^2\theta)^{\frac{1}{2}} + M_1\cos\theta}{M_2 + M_1}\right]^2 \tag{4.4}$$

The kinematic factor depends only on the ratio of the projectile to the target masses and on the scattering angle θ. One sees from Eq. (4.4) that for any combination of projectile and target mass K always has its lowest value at 180^0. The value there is

$$K(\theta = 180^0) = [(M_2 - M_1)/(M_2 + M_1)]^2 = [(1-x)/(1+x)]^2 \tag{4.5}$$

In practice, when a target contains two types of atoms that differ in their masses by a small amount ΔM_2, it is important that this difference produces as large a change ΔE_1 as possible in the measured energy E_1 of the projectile after the collision. As Eq. (4.4) shows, a change of ΔM_2 (for fixed M_1) gives the largest change of K when $\theta = 180^0$ for all but the smallest values of M_2. Thus $\theta = 180^0$ is the preferred location for the detector. To place a detector exactly at $\theta = 180^0$ is not possible because the detector would obstruct the path of the incident particles. The detector is thus normally positioned at some steep backward angle, such as 170^0. In quantitative terms, ΔE_1 and ΔM_2 are related to each other by

$$\Delta E_1 = E_0\left(\frac{dK}{dM_2}\right)\Delta M_2 \tag{4.6}$$

In the vicinity of $\theta = 180^0$ i.e., $\theta = \pi - \delta$, (where δ measures the deviation of θ from π in units of arc), K is very closely approximated by (for $M_2 >> M_1$, which is most often the)

$$\Delta E_1 = E_0(4 - \delta^2)\frac{M_1}{M_2^2}\Delta M_2 \tag{4.7}$$

Every practical detection system has a finite resolution. If ΔE_1 falls below this limit, the distinction between two masses is lost. To obtain good mass resolution, it is therefore desirable that the coefficient of ΔM_2 be as large as possible.

4.2.2 . Scattering Cross Section

Let a narrow beam of fast particles impinge on a thin uniform target that is wider than the beam. At an angle θ from the direction of incidence, let an ideal detector count each particle scattered in the differential solid angle dΩ (see Fig. 4.3). If Q is the total number of particles that have hit the target and dQ is the number of particles recorded by the detector, then the differential scattering cross section dσ/dΩ is defined as

$$\frac{d\sigma}{d\Omega} = \left(\frac{1}{Nt}\right)\left[\left(\frac{dQ}{d\Omega}\right)/Q\right] \tag{4.8}$$

where N is the volume density of atoms in the target and t is its thickness. Thus Nt is the number of target atoms per unit area.

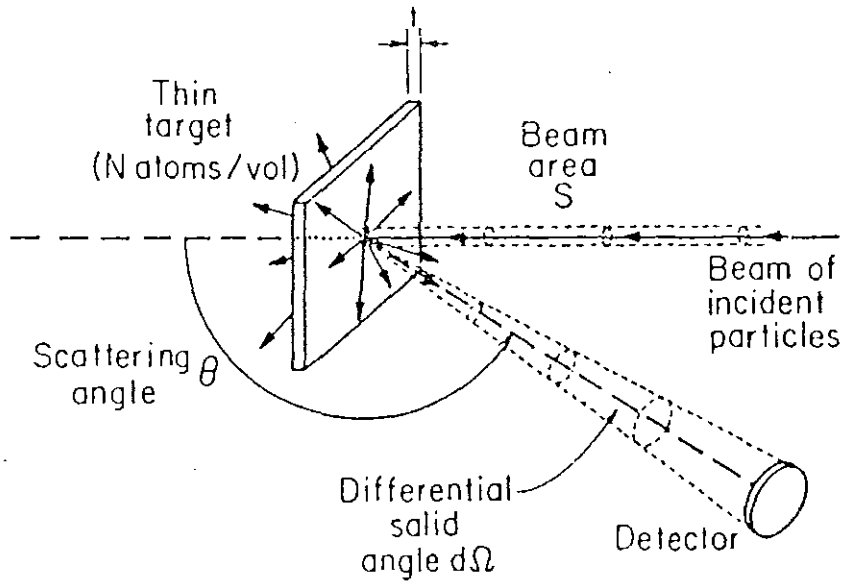

Fig. 4.3 Layout of a scattering experiment to demonstrate the concept of the differential cross section

The differential scattering cross section $d\sigma/d\Omega$ has the dimension of an area ("cross section") whose meaning is based on a geometrical interpretation of the probability that the scattering will result in a signal at the detector. One imagines that each nucleus presents an area $d\sigma/d\Omega$ to the beam of the incident particles. It is also assumed that this area is quite small and that the atoms within the target are randomly distributed in such a way that the differential cross sections $d\sigma/d\Omega$ of the nuclei do not overlap. Let s be the surface area of the target illuminated uniformly by the beam. Then the total number of atoms eligible for a scattering collision in the target is sNt. The ratio of the total cross-sectional area of all eligible atoms $sNtd\sigma/d\Omega$ to the area s actually exposed is then interpreted as the probability that the scattering event will be recorded by the detector; that is, this ratio is set equal to $(1/d\Omega)dQ/Q$. Equation (4.8) then follows.

To calculate the differential cross section for an elastic collision, the principles of conservation of energy and momentum must be complemented by a specific model for the force that acts during the collision between the projectile and the target nucleus. In most cases, this force is very well described by the Coulomb repulsion of the two nuclei as long as the distance of the closest approach is large compared with nuclear dimensions, but small compared with the Bohr radius. When these assumptions are made, the differential scattering cross section is given by Rutherford's formula [10]

$$\left(\frac{d\sigma}{d\Omega}\right)_C = \left[\frac{Z_1 Z_2 e^2}{4E_C \sin^2(\theta_C/2)}\right]^2 \tag{4.9}$$

where the subscript c indicates that the values are given with respect to the center-of-mass coordinates. Here Z_1 is the atomic number of the projectile atom with mass M_1, Z_2 is the atomic number of the target atom with mass M_2, e is the electronic charge, and E is the energy of the projectile immediately before scattering. For the general case, the

transformation of this formula from the center-of-mass to the laboratory frame of reference yields [16]

$$\frac{d\sigma}{d\Omega} = \left(\frac{Z_1 Z_2 e^2}{4E}\right)^2 \frac{4}{\sin^4\theta} \frac{\left\{\left[1 - ((M_1/M_2)\sin\theta)^2\right]^{1/2} + \cos\theta\right\}^2}{\left[1 - ((M_1/M_2)\sin\theta)^2\right]^{1/2}} \tag{4.10}$$

4.3. Depth Scale for an Elemental Sample

This section describes how one relates the energy E_1 of the detected particle to the depth x at which the backscattering event occurs in a monoisotopic elemental sample. In Fig. 4.4 the energy of the incident particles is E_0, the energy immediately before scattering at a depth x is E, and the energy of the particle emerging from the surface is E_1. The scattering angle in the laboratory frame of reference is given by $\theta = 180^0 - \theta_1 - \theta_2$, where θ_1 and θ_2 are the angles between the sample normal and the direction of the incident beam and of the scattered particle, respectively.

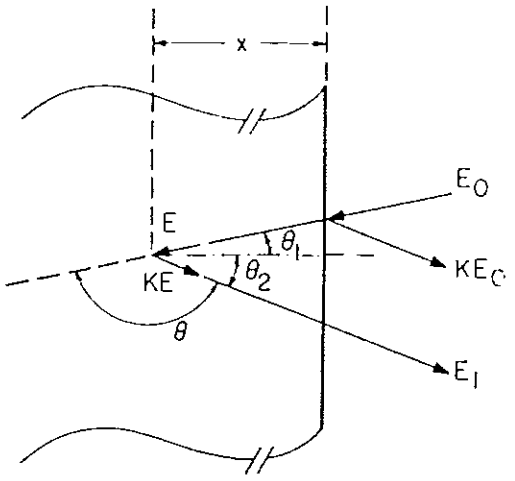

Fig. 4.4 Symbols used in the description of backscattering events in a sample consisting of a monoisotopic element.

We can relate the energy E to the length $x/\cos\theta_1$ of the incident path by

$$\frac{x}{\cos\theta_1} = -\int_{E_0}^{E} dE / \left(\frac{dE}{dx}\right) \tag{4.11}$$

where the negative sign arises because E is smaller than E_0 and dE/dx is taken as a positive quantity. Similarly, the path length $x/\cos\theta_2$ of the outward path is related to KE and E_1 by

$$\frac{x}{\cos\theta_2} = -\int_{KE}^{E_1} dE / \left(\frac{dE}{dx}\right) \tag{4.12}$$

A graphical interpretation of these two equations is given in Fig. 4.5. Part (a) shows dE/dx as a function of energy as a light line. The heavy segments give the dE/dx values for the inward path from E_0 to E and for the outward path from KE to E_1. The difference E_0-E is the energy loss along the inward path ΔE_{in};similarly, KE-E_1 is the energy loss along the outward path ΔE_{out}.

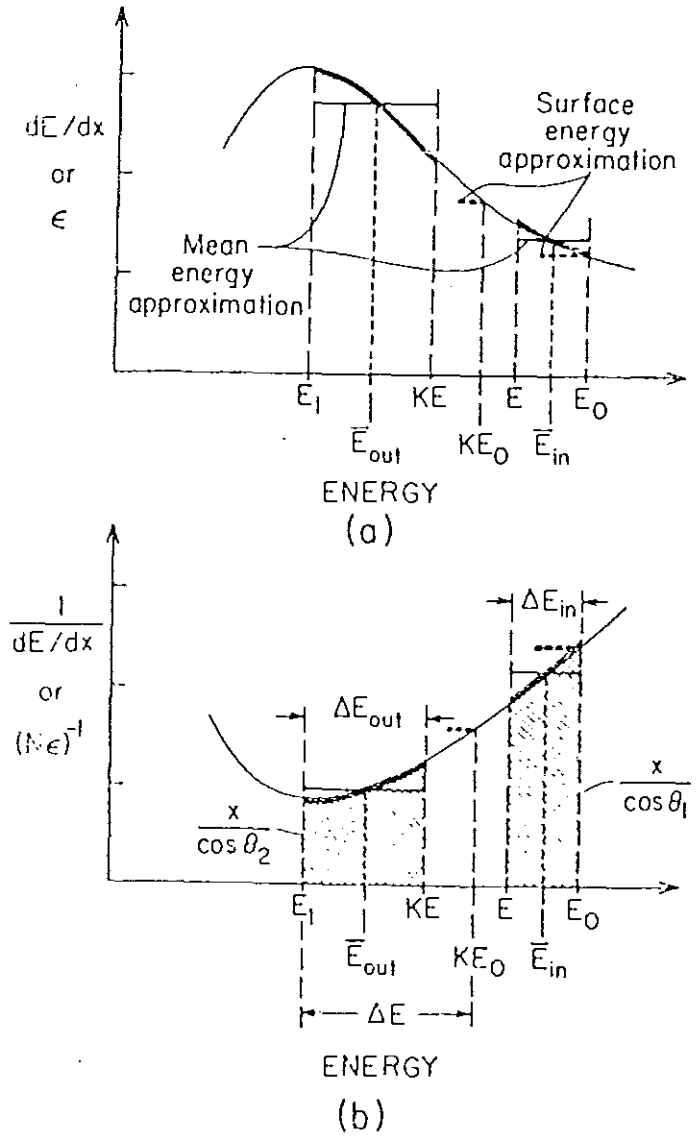

Fig. 4.5 Graphical representation of the energy loss of particles along their inward and outward paths (heavy line) through a sample consisting of a monoisotopic element.

According to Eqs. (4.11) and (4.12), it is the reciprocal of dE/dx that must be integrated over these two segments. This reciprocal curve is shown in part (b) of Fig. 4.5, with the heavy segments again indicating values for the inward and outward paths. By Eqs. (4.11) and (4.12), the two shaded areas give the path lengths $x/\cos\theta_1$ for the inward path and $x/\cos\theta_2$ for the outward path. If $\theta_1 = \theta_2$, these two areas are exactly equal.

To relate the energy E_1 of the detected particle to the depth x at which the backscattering event occurs, it is necessary to find the value of the shaded areas. The problem is that the energy E before scattering is not an experimentally accessible quantity, but E_0 and E_1 are. One thus has to find x in terms of E_0 and E_1. There are three ways of doing this:

1. Use tabulated values of dE/dx and execute the integrations numerically to find corresponding sets of E and x, and subsequently KE and E_1.

2. Assume that dE/dx is constant over each path. Equations (4.11) and (4.12) can then be integrated and E can be obtained

3. Assume some functional dependence for dE/dx. Matching pairs of E and x and of x and E_1 can then be obtained analytically.

4.3.1. Energy Loss Factor and Stopping

Cross Section Factor

If one assumes a constant value for dE/dx along the inward and outward paths, the two integrals in Eqs. (4.11) and (4.12) reduce to

$$E = E_0 - \frac{x}{\cos\theta_1}\left(\frac{dE}{dx}\right)_{in} \tag{4.13}$$

and

$$E_1 = KE - \frac{x}{\cos\theta_2}\left(\frac{dE}{dx}\right)_{out} \tag{4.14}$$

4.4. Depth Scale for a Compound

To relate the energy E_1 of the detected particle to the depth x at which the backscattering event occurs, we follow the formalism described in Section 4.3. for the depth scale of an elemental target. We use a subscript to indicate the atom struck, so that E_{1A} and E_{1B} denote the energies of detected particles scattered from atoms A and B, respectively. Superscripts are used to denote the stopping medium, so that ε^{AmBn} is the stopping cross sections of a material containing elements A and B in the atomic ratio m/n. It is preferable to use the notation ε^{AB} instead of ε^{AmBn}, even if m and n are not unity. Then ε^{AB} is given by [15]

$$\varepsilon^{AB} = m\varepsilon^{A} + n\varepsilon^{B} \tag{4.21}$$

A particle penetrating the sample to a depth x undergoes an energy loss ΔE_{in} along the inward path given by

$$\Delta E_{in} = \left(N^{AB}\frac{x}{\cos\theta_1}\right)\varepsilon_{in}^{AB} \tag{4.22}$$

where N^{AB} is the number of molecules A_mB_n per unit volume. The energy loss ΔE_{out} along the outgoing path depends on the collision partner. Therefore, the energy difference ΔE between particles scattered at the front surface and at a depth x can have two values, ΔE_A or ΔE_B depending on whether the particles scatter from atom A or atom B. In analogy with the result in Section 4.3 for an elemental sample, we thus have

$$\Delta E_A = [\varepsilon]_A^{AB} N^{AB} x \tag{4.23}$$

and

$$\Delta E_B = [\varepsilon]_B^{AB} N^{AB} x \tag{4.24}$$

where

$$[\varepsilon]_A^{AB} = \frac{K_A}{\cos\theta_1}\varepsilon_{in}^{AB} + \frac{1}{\cos\theta_2}\varepsilon_{out,A}^{AB} \tag{4.25}$$

$$[\varepsilon]_B^{AB} = \frac{K_B}{\cos\theta_2}\varepsilon_{in}^{AB} + \frac{1}{\cos\theta_2}\varepsilon_{out,B}^{AB} \tag{4.26}$$

5. Experimental Results and Discussion

5.1. Low Dose Implantation of Ti into $LiNbO_3$

Implantation of Ti followed by oven annealing of $LiNbO_3$ has been investigated since the late 1980's and remarkable results have been found, especially comparing the conventionally grown Ti- indiffused $LiNbO_3$ waveguide (9 hour at 1000^0C) and Ti-implanted $LiNbO_3$ and oven annealed (1 hour at 1000^0C) waveguide [3,17-20]. But Ti implanted on $LiNbO_3$ and Rapid Thermal Annealing (RTA, 1 minute at 1060^0C) has never been reported up to now. In this section oven annealing and rapid thermal annealing of Ti-implanted $LiNbO_3$, for different doses, are compared.

Ti^{2+} ions were implanted on the same optical grade x-cut $LiNbO_3$ samples, with a size of 0.5x0.5 cm^2. The implantation doses were 10^{15} Ti/cm^2 and 10^{16} Ti/cm^2 (relatively low doses) and the energy of the ions was 400 keV. Prior to the implantation, the area of the beam spot was carefully noted, and then the samples were securely clamped against a copper backplate, covering almost half part of the samples' area by the clamps so that the unimplanted region could be used to search for channels during RBS measurements. The implanted samples were analyzed with Rutherford backscattering spectrometry (RBS), having He^+ ions as the analyzing beam with an energy of 1.4 MeV. The as-implanted spectra (spectra measured after implantation without annealing) of a sample is shown in Fig. 5.1. The random spectrum is measured in a random direction, however, the channeling spectrum is measured in a certain crystallographic direction. If the sample is a crystal then during channeling measurement, the He^+ ions go through the channel and one will get very low yield of the channeling spectrum. In Fig. 5.1, due to the low Ti concentration, the small Ti signal is buried in the Nb signal and cannot be resolved for analysis. For Ti:$LiNbO_3$ system, since the heaviest atom is Nb, the high energy edge of the spectrum is located at

$E=K_{Nb}E_0$. The He ion beam has an energy E_0=1.4 MeV and K_{Nb}=0.8429 (for θ =170^0), hence E= 1.18 MeV. To get the channel number corresponding to this energy value we assume a linear relationship between the energy values and the channel numbers which is given by the equation

$$E = E_{off} + n\xi$$

where ξ (=1.39 keV/channel) is energy per channel or the slope of the straight line, E_{off} (=50.80 keV) is an energy offset and n is the channel number. Then, from the above equation, the channel number n will be about 815 for E=1.18 MeV.

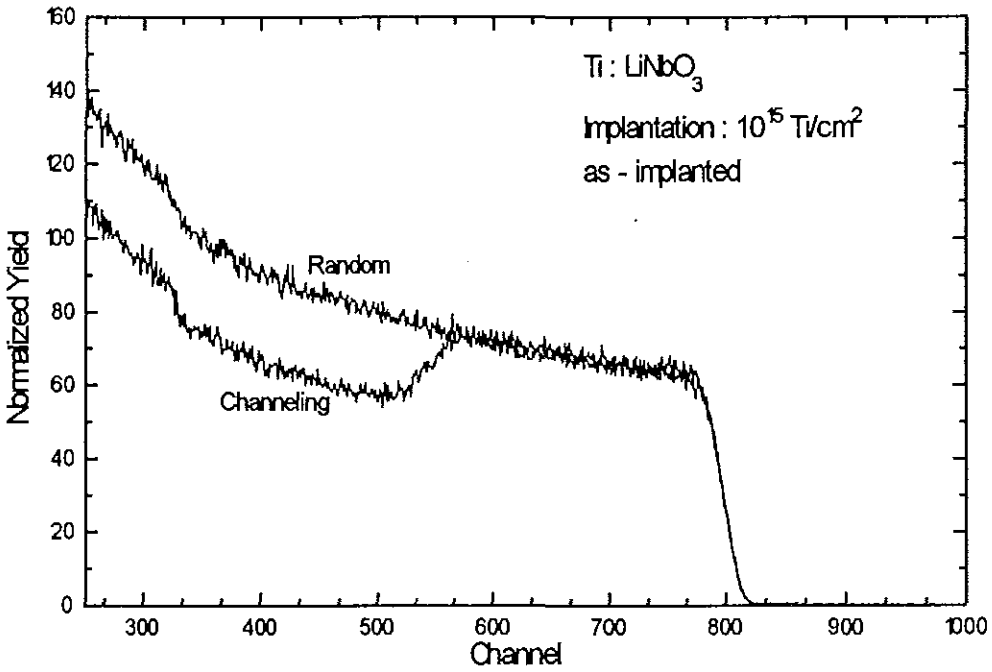

Fig. 5.1 As - implanted random and channeling spectra of a sample

However, Fig. 5.1. shows a very strange behavior. At the top of the spectrum, the surface edge has shifted considerably from the usual spectrum to the left (the spectra are not sharp at channel number 815). It seems that there was charging of the sample during RBS measurement. If the He ion beam is far from the discharging clamps during measurement, since $LiNbO_3$ is insulator, the He ions will be accumulated on the target, the effect being repulsion of the incoming beam. If we focus the He ion beam near the

discharging clamps, in order to avoid accumulation of the He ions on the samples, then the high energy edge of the spectrum is given by Eq. (4.4)

$$E = KE_0$$

But if the He ion beam is far from the clamps then charges will be accumulated on the sample. So, when the He ions are approaching the target they will be repelled by the already accumulated charges. Therefore the energy E_0 decreases to

$$E_0' = E_0 - \Delta E$$

Then the high energy edge will be at

$$E' = KE_0' + \Delta E = KE_0 - K\Delta E + \Delta E = KE_0 + (1-K)\Delta E$$

ΔE is added at the above expression because the backscattered He ions will also be accelerated away from the target by the accumulated charges. Since (1-K) > 0 then the high energy edge is increased. Therefore the reason for the shift of the high energy edge to the left can not be due to charging of the sample during measurement.

Upon exposure to the atmosphere the implanted surfaces became cloudy within a few hours or days depending on the condition of exposure. This cloudy appearance was due to the formation of surface precipitates. Since the structure of $LiNbO_3$ is mostly sustained by Nb-O bonds and only to a much smaller extent by Li-O bonds, the damage to implantation sets some Li free and the highly mobile Li-atoms precipitate to the surface, and the crystal will have a deficiency of Li in the near surface over the range of the implanted region. Hence, the decrease of the high energy edge is due to the Li- precipitate on the surface of the sample. The Li- precipitate can easily be cleaned by water and propanol. The spectrum of a sample before and after cleaning is compared in Fig. 5.2. Moreover, B.R. Appleton and et al. [21] reported that as long as crystals remained in vacuum after implantation at least for times up to 30 hrs, the implanted surfaces retained their shiny appearance. Some samples were also measured immediately after implantation which showed a perfect high energy edge. But exposing Ti implanted $LiNbO_3$ to normal air

for several days results in the formation of soapy-like surface deposit because the surface agglomerate contained large amounts of Li. It seems possible that Li might be displaced during the room temperature implantation, transported to the surface by radiation-enhanced diffusion and diffused out of the samples by chemical interaction with the atmosphere. From the spectra we see that the high energy edge becomes sharp after

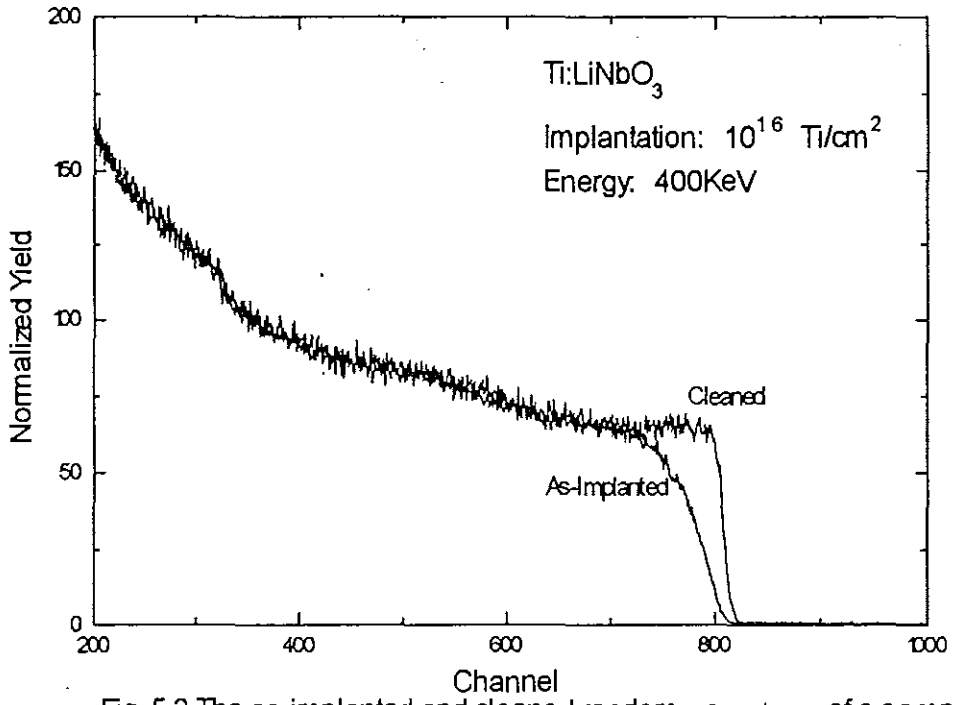

Fig. 5.2 The as-implanted and cleaned random spectra of a sample

cleaning, indicating that the Li- precipitate has been removed.

Theoretical simulations can be done to obtain the distribution of ions in solids. Fig.5.3 shows a TRIM simulation of Ti implantation on $LiNbO_3$ with an energy of 400 keV which gives an impression about the correlation between depth and Ti- concentration. TRIM is a Monte-Carlo simulation program designed for ion implantation where one inputs only the implantation energy, the ion species and the composition of the target and gets an output of the distribution of the implanted ions. In the graph the Ti- concentration is in arbitrary units having values such that the area under the curve is normalized. The Ti-

distribution is Gaussian which depends only on the implantation energy for a ion-target combination. For 400 keV, the range of the deepest implanted ions is arc nm and the peak concentration is at about 240 nm which do not depend on the imp dose. The effect of the implantation dose is to change the values of the y-axis.

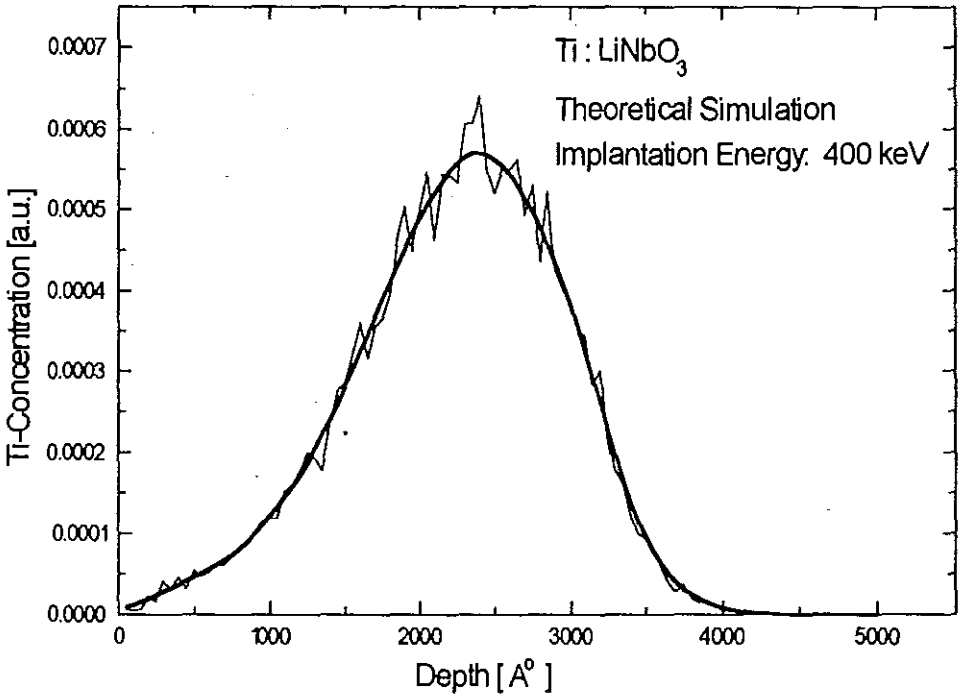

Fig. 5.3 Computer simulation of the Ti profile after implantation

For any implantation dose N the conversion factor for a new y-axis, Y is:

$$Y = yN \times 10^8 / cm$$

If N is in Ti/cm^2 then Y will be in Ti/cm^3. Let us look at the as-implanted s of Ti:$LiNbO_3$, see Fig. 5.1. Since the random and channeling spectra overlap to a depth then the crystal is completely amorphized due to the implantation proce amorphized region is around 400 nm which is estimated from the overlap of spectra using RUMP (computer simulation program designed to analyze measured of RBS). Although TRIM assumes amorphous $LiNbO_3$, it gives a good and impression about the distribution of the implanted ions.

800°C) to remove all residual damage produced by the implantation, to bring the implanted Ti into registry with the lattice, and to restore crystallinity all the way up to the surface. Unfortunately, high annealing temperatures also favor Ti diffusion, a huge amount will be carried towards the surface.

From the TRIM simulation (see Fig. 5.3), we have seen that the as-implanted Ti-profile has a full Gaussian distribution centered at 240 nm, with a FWHM of 160 nm and implanted region of 400 nm. In order to know the depth profile of the Ti after annealing in the RTA at 1060°C for 1 minute, SIMS (Secondary Ion Mass Spectrometry- by bombarding the sample with O_2^+ , Ti ions are ejected from the surface of the sample and detected) measurement of a sample, implanted with a dose of 10^{16} Ti/cm^2, has been carried out and the result is shown in Fig.5.6. The spectrum shows that the Ti has diffused to the

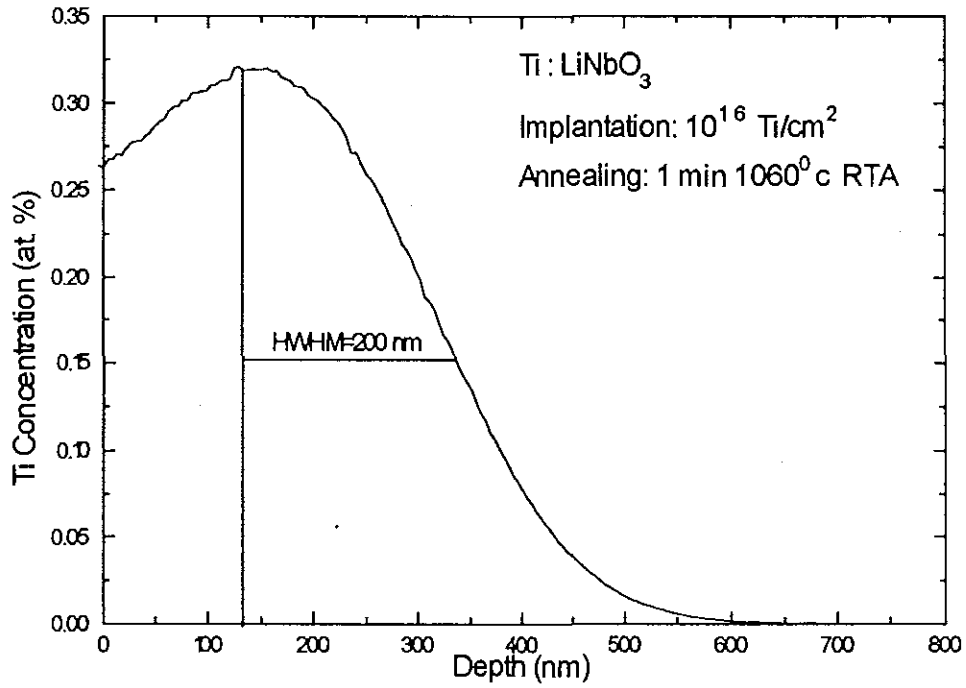

Fig. 5.6 Titanium profile, as measured by SIMS, of RTA annealed sample

surface and became only half Gaussian. This is due to the implantation damage over the implanted region which allows higher ion mobilities, i.e., the damaged (amorphized) region

5.3 High-Dose Ti Implantation of $LiNbO_3$ and Annealing

In the low dose implantation we have seen that the crystal $LiNbO_3$ becomes amorphous up to a certain depth starting from the surface. The depth of the amorphized region depends only on the energy of the ions, it does not depend on the implanted dose. In the high-dose implantation one gets more Ti- ions over the implanted region. Fig 5.8 shows

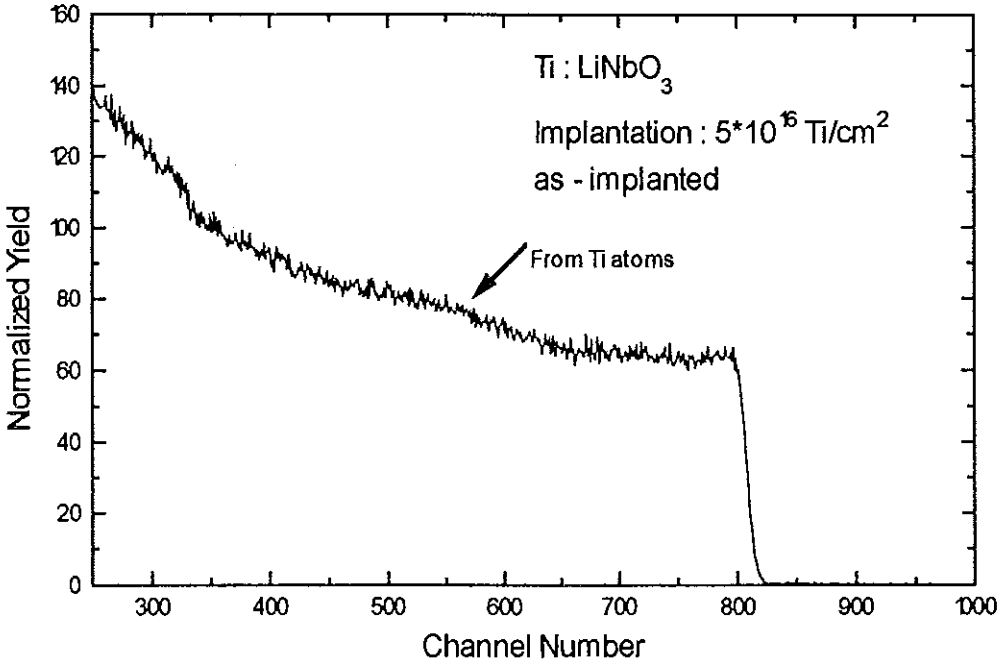

Fig. 5.8 As - implanted random spectrum of a sample

the as-implanted random spectrum of a sample implanted with a dose of $5x10^{16}$ Ti/cm^2 and an energy of 400 keV. The Ti profile is visible starting from channel number 450 up to 600, as shown in the figure. The addition of Ti into the crystal is reflected not only by the increase of the yield in the region from channel 450 to channel 600 but also by the decrease of the yield from channel number 650 to 800. Due to the stoichiometric change after implantation, the relative concentration of Nb is decreased over the implanted region which causes depression of the spectrum from channel number 650 to 800, i.e the yield from the Nb atoms around the near surface region. This effect is more pronounced for higher dose

implantation. Even though the Ti profile is visible in Fig. 5.8, it is still buried partly in the Nb signal and cannot be resolved for analysis using RBS. After implantation, some of the samples were annealed with RTA (for 1 minute at 1060^{0}C) and some of them with oven (for 1 hour at 1060^{0}C). In both annealing processes, perfect recovery of crystallinity with minimum yields around 2% was achieved. The Random and channeling spectra of RTA annealed sample is shown in Fig. 5.9. The spectra show that the sample recrystallized with

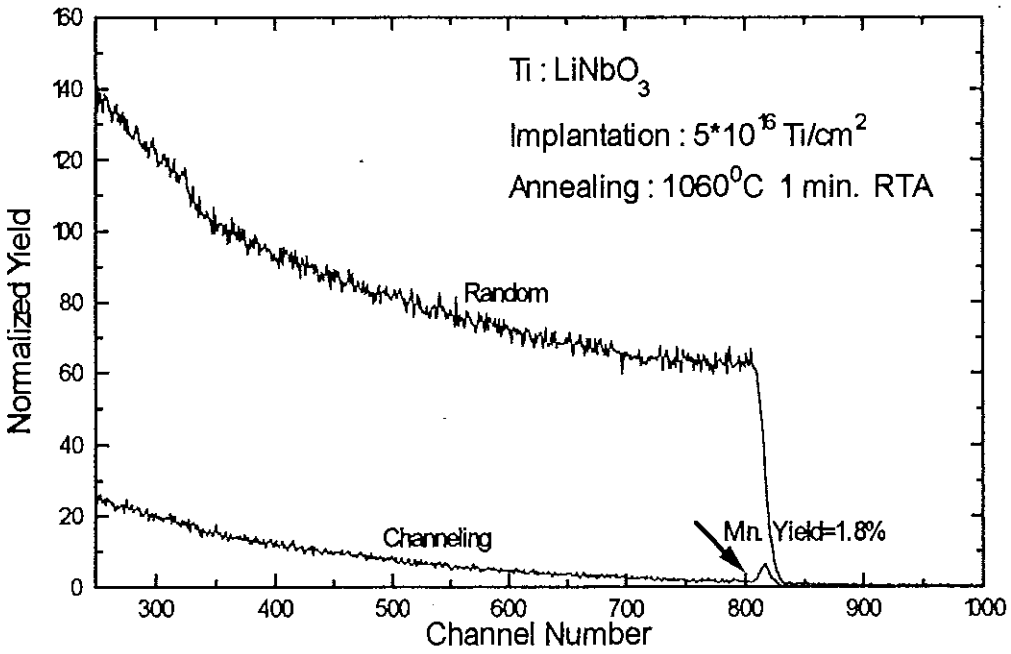

Fig. 5.9 Random and channeling spectra of RTA annealed sample

a minimum yield of 1.8%, a typical value for unimplanted crystals of $LiNbO_3$. To know about the Ti profile after RTA annealing, SIMS measurement of the sample was done, Fig. 5.10. Due to the high temperature annealing, the Ti ions diffused to the surface and the full Gaussian of the as- implanted Ti profile becomes almost half after annealing the sample. The HWHM (~0.23 μm) of the high dose implanted sample ($5x10^{16}$ Ti/cm^2) is a little bit wider than that of the low dose implanted sample (10^{16} Ti/cm^2), because the higher the Ti concentration, the higher will be the diffusion of the Ti atoms and hence broadening the Gaussian profile of the Ti.

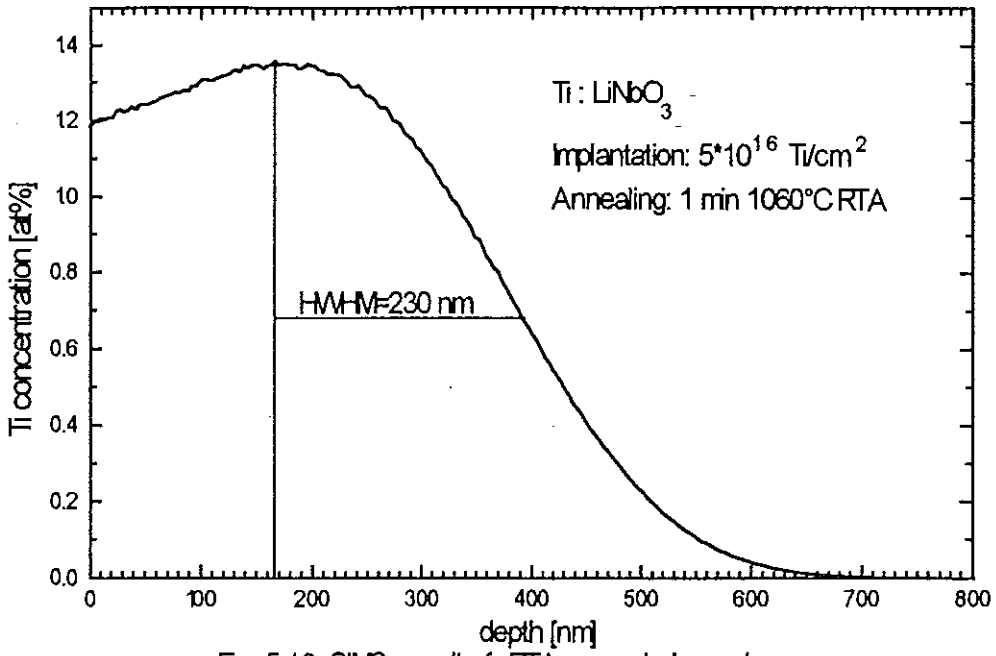

Fig. 5.10 SIMS result of RTA annealed sample

Samples were also implanted even with higher doses (of 10^{17} Ti/cm^2) and annealed with RTA and oven, analyzed with RBS and SIMS. Fig. 5.11 shows the as- implanted spectrum of a sample implanted with a dose of 10^{17} Ti/cm^2 and energy of 400 keV.

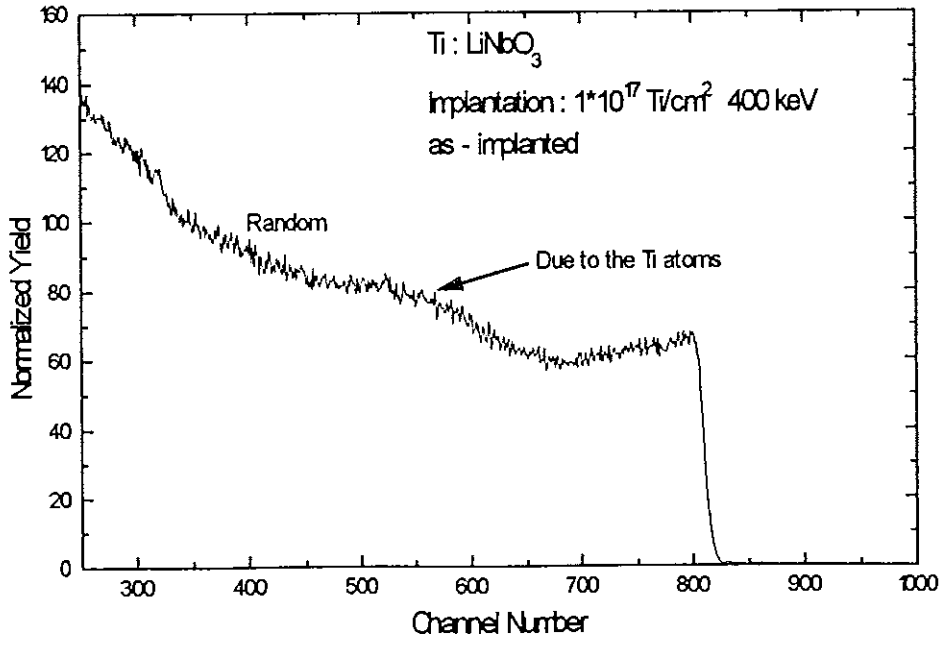

Fig. 5.11 As - implanted random spectrum of a high dose implanted sample

For this dose, the as- implanted spectrum shows more clearly the Ti signal and the depression of the Nb signal over the implanted region. However, it remains still difficult to determine the depth profile of the Ti using RUMP due to the overlap of the Nb and Ti signals. Then the sample was annealed with RTA for 1 minute at 1060°C. The random and channeling spectra of this RTA annealed sample is shown in Fig. 5.12.

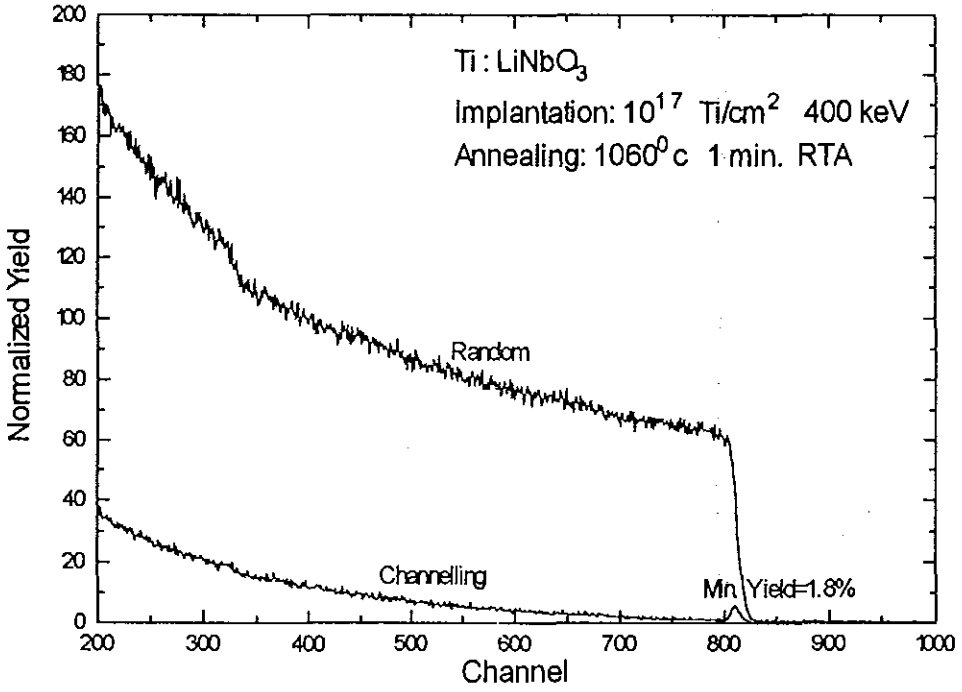

Fig. 5.12 The random and channelling spectrum of RTA annealed sample

The sample recrystallized with a minimum yield of 1.8%. Hence, after implanting samples with doses up to 10^{17} Ti/cm^2 it is possible to restore crystallinity by annealing in the RTA only for one minute at 1060°C. The oven annealing also restores crystallinity at this temperature after 1 hour but the HWHM of the Gaussian distribution of the Ti profile becomes very wide compared to that of the RTA annealed samples.

The SIMS measurement of a sample implanted with 10^{17} Ti/cm^2 and annealed in the RTA for 1 minute at 1060°c is shown in Fig. 5.13. The HWHM of the Gaussian is about 0.35 μm and the maximum concentration of the Ti (about 3 at.%) is located at the surface.

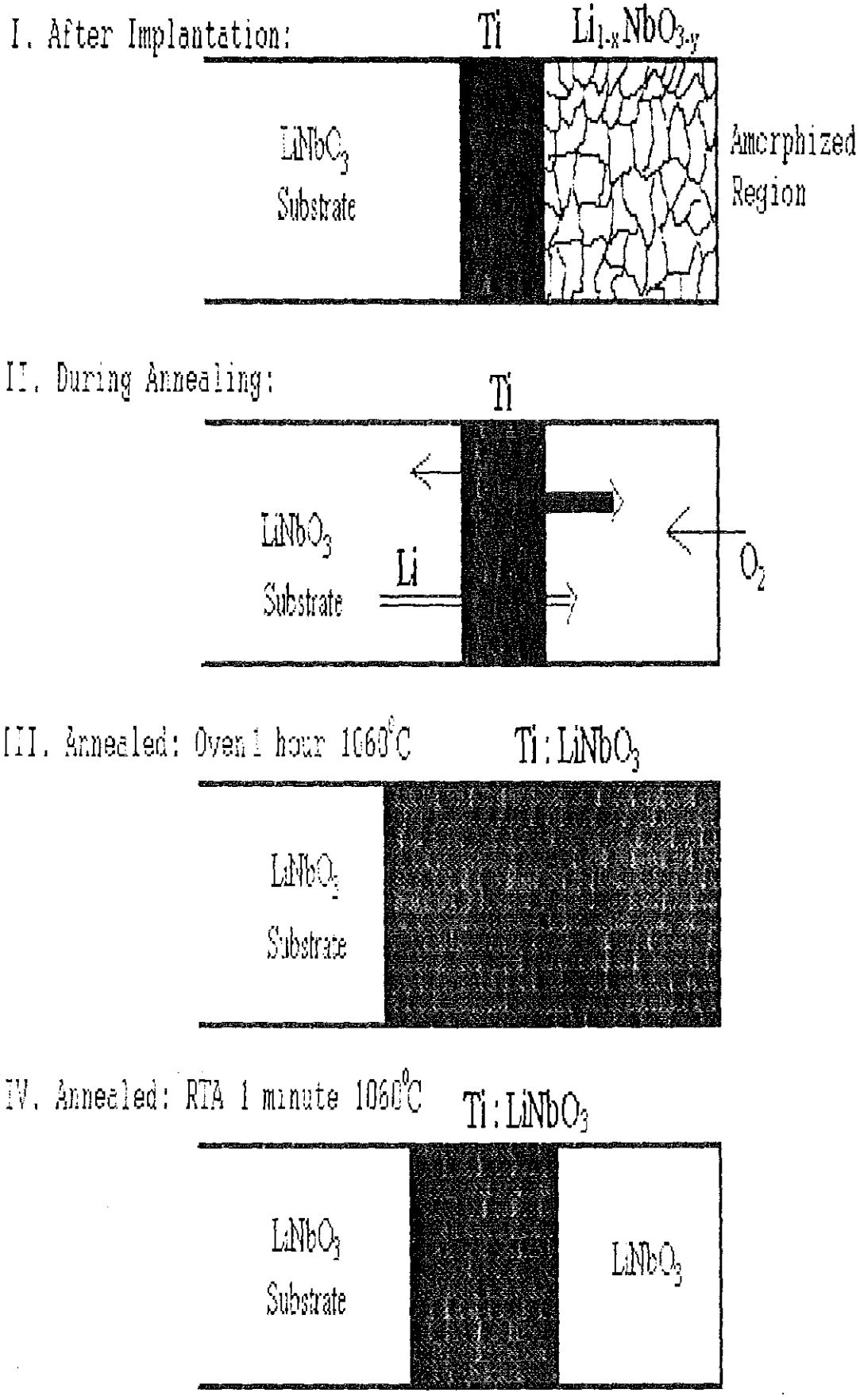

Fig. 5.15 Diagrammatic representation of implantation and annealing processes

towards the surface than to the bulk due to the radiation damage over the implanted region. The third diagram shows the Ti profile of an oven annealed sample extending up to the surface, and the fourth diagram shows the RTA annealed sample with a buried Ti- profile inside the $LiNbO_3$ crystal.

5.4. Ti Implantation and Annealing of Al_2O_3

In 1982 researchers at Lincoln Laboratory operated a tuneable laser based on $Ti:Al_2O_3$ for the first time [24]. A wide variety of developments in $Ti:Al_2O_3$ laser technology then followed the advances in crystal growth that occurred during the mid 1980s. Since that time researchers have demonstrated high efficiency, wide tunability frequency- stable continuous- wave operation, and generation of short pulses ($< 10^{-3}$sec.) with $Ti:AL_2O_3$ lasers. They are now commercially available and are a valuable research tool in many laboratories. Titanium- doped sapphire laser has the largest tuning range than any other laser (from 660 to 1180 nm). The substitutional Ti^{+3} ion in Al_2O_3 retains one d electron which is responsible for color (absorption) and laser action. However, several attempts to implant Ti into Al_2O_3 for the fabrication of Ti: sapphire wave guide laser have failed, since a sufficient epitaxial regrowth of the sapphire could not be established [25].

In this work we present results from RBS measurements of different annealing methods performed on Ti- implanted Al_2O_3 with an implantation energy of 400 keV and doses of 10^{15}, 10^{16}, $5x10^{16}$, 10^{17} Ti/cm^2. During implantation, it has been observed that some crystalline materials maintain their crystallinity to very high doses ($> 10^{17}$ ions/cm^2), whereas others are rendered amorphous at relatively low doses ($LiNbO_3$, Si). Ion implantation of Al_2O_3 at room temperature or above gives rise to extensive damage in the near- surface region, but this region remains crystalline during ion bombardment unless very high doses are used [26]. Following implantation, the near surface remains crystalline, and

The spectra of a sample implanted with a dose of $5x10^{16}$ Ti/cm^2 is shown in Fig. 5.17. The yield of the channeling spectrum of the implanted sample is higher than that of the unimplanted spectrum. This indicates that the crystal has got probably tangled array of dislocations due to the implantation damage. For the unimplanted crystal, the surface peak

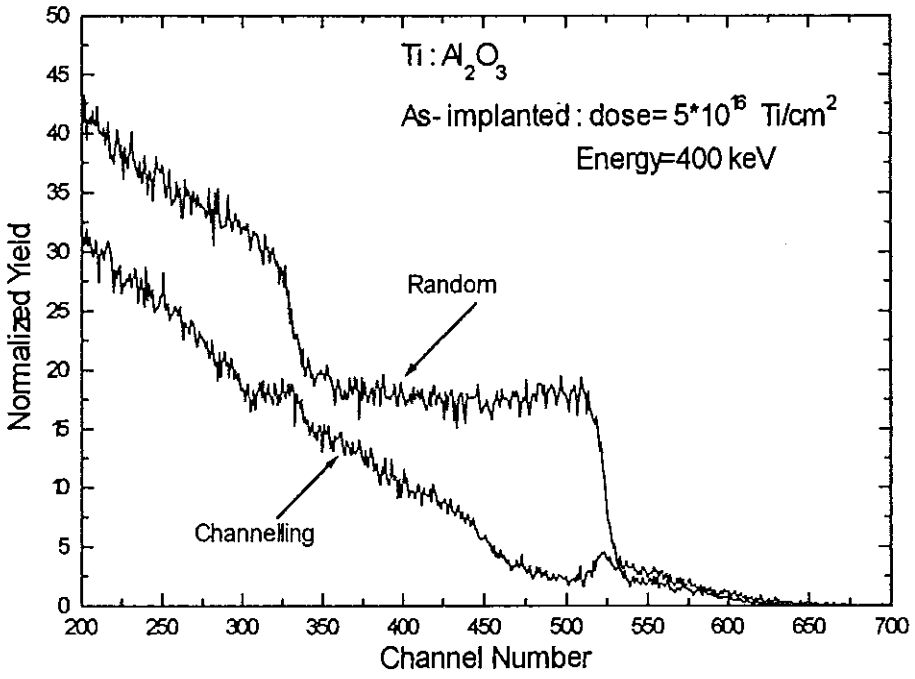

Fig. 5.17 As- implanted random and channelling spectra of a sample

(in Fig. 5.16) of the Al atoms is at about channel number 520, hence the signal beyond this channel number is due to the implanted Ti atoms. Therefore, the Ti profile can easily be distinguished and simulated with RUMP. The simulation of the random spectrum of Fig.5.17 is shown in Fig.5.18. For simulation the following five layers were used

1). 130 nm composition of Al_2O_3

2). 50 nm composition of $Al_{1.93}O_3Ti_{0.07}$

3). 80 nm composition of $Al_{1.88}O_3Ti_{0.12}$

4). 50 nm composition of $Al_{1.93}O_3Ti_{0.07}$

5). 3000 nm composition of Al_2O_3

The subscripts are simply relative numbers chosen to fit the spectrum and to give a total sum of 5 because the unimplanted Al_2O_3 contains five atoms. With this layers RUMP assumes a homogeneous stoichiometry and calculates the concentration of Ti over the

implanted depth using the density of sapphire ($1.175x10^{23}$ atoms/cm^3). Thickness, as measured by RBS, is really density, not distance. A conversion from atoms/area to distance is possible only if the density of the film (atoms/volume) is known.

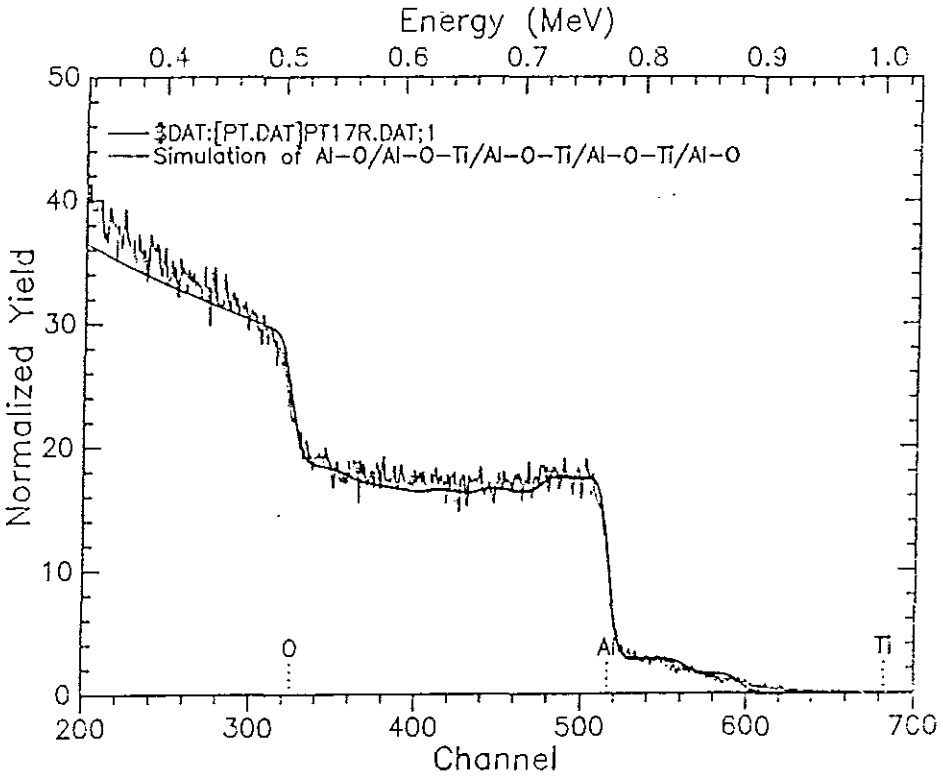

Fig. 5.18 RUMP simulation of a sample implanted with 5x 10^{16} Ti/cm^2

For the first and fifth layers the configuration is only Al_2O_3 we do not have any Ti. The idea behind this assumption is that by considering a Gaussian distribution after implantation inside the sample such that the surface region will not have any Ti ions and the last layer corresponds to the substrate where the Ti ions could not reach. For the second and fourth layers the stoichiometry is $Al_{1.93}O_3Ti_{0.07}$ then the Ti concentration will be

$$1.175 \times 10^{23} atoms/cm^3 \times \frac{0.07}{5} = 1.65 \times 10^{21} atoms/cm^3$$

and for the third layer the stoichiometry is $Al_{1.88}O_3Ti_{0.12}$, the Ti concentration will be

$$1.175 \times 10^{23} atoms/cm^3 \times \frac{0.12}{5} = 2.82 \times 10^{21} atoms/cm^3$$

In addition to the RBS measurement, to get an impression about the correlation between depth and Ti- concentration, a theoretical simulation has been done. The TRIM simulation of Ti implantation on Al_2O_3 with an energy of 400 keV is shown in Fig. 5.19.

simulation of Ti implantation on Al_2O_3 with an energy of 400 keV is shown in Fig. 5.19. For comparison the layers from the RUMP simulation are also drawn. The values of the

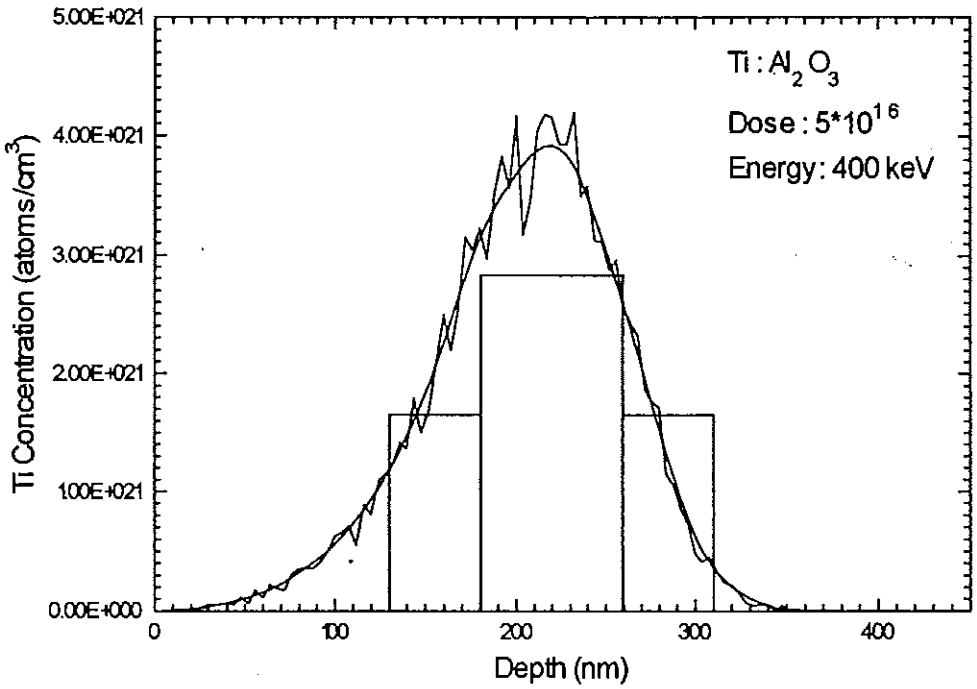

Fig. 5.19 TRIM simulation of Al_2O_3. The layers are from RUMP simulation

ordinate are set such that the area under the TRIM simulation gives the implanted dose of $5x10^{16}$ Ti/cm^2. However, the total area of the rectangular layers is about $3.9x10^{16}$ Ti/cm^2. Even though this value is far from the exact dose, the distribution of the Ti ions is almost similar with that of the TRIM simulation. Both, the RBS measurement (followed by RUMP simulation) and the TRIM simulation estimate almost the same value for the range of the deepest implanted ions ~ 350 nm.

Then, after implantation the samples were annealed with the following different annealing methods and conditions

-RTA at 1060^{0}C for 1 min.

-RTA at 1150^{0}C for 4x30 sec.(annealing for a total of 2 min. but in steps)

-Oven annealing at 1060^{0}C for 1 h.

-High temperature furnace annealing (HTF) at 1400^{0}C for 1 h.

Because of the very high melting point of sapphire (~1800°C) [26], annealing the samples at a temperature of 1060°C does not change the as- implanted spectrum much. But annealing at 1150°C changes the channeling spectrum. Fig.5.20 shows the spectra of a sample implanted with a dose of 10^{16} Ti/cm^2 and annealed with RTA at 1150°C for four times 30 sec (annealing step done with four steps).

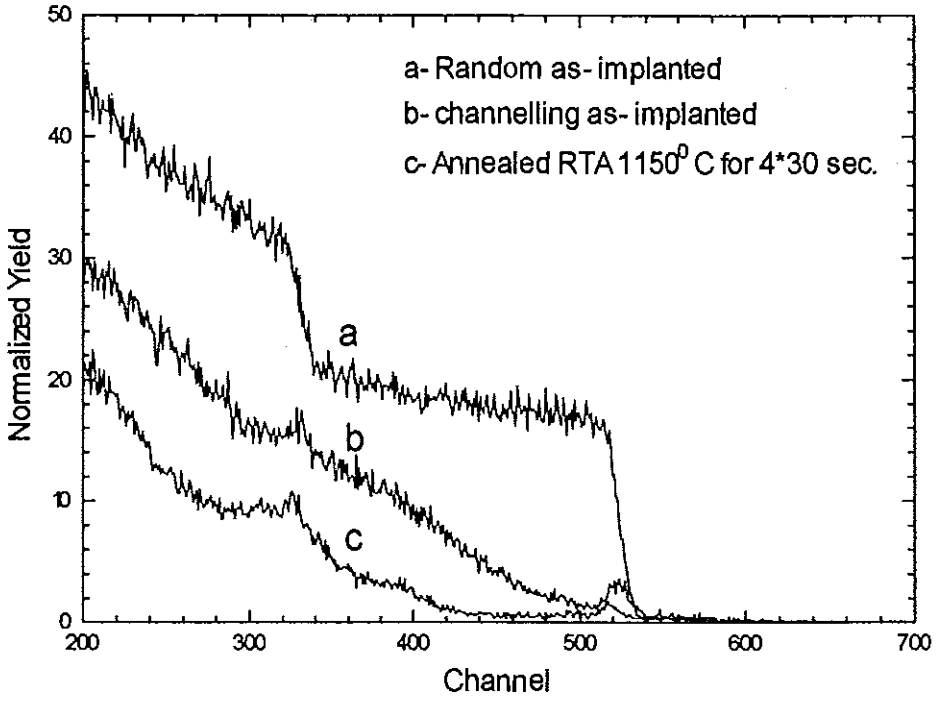

Fig. 5.20 RBS and channelling spectra of a sample implanted with 10 ^{16} Ti/cm^2 and RTA annealed at 1150 °C for 2 minutes

In Fig. 5.20, the channeled spectrum of the annealed sample lowered significantly indicating better crystallinity than the as- implanted sample. However, the spectra also shows that Ti ions do not diffuse in sapphire at this temperature, i.e., there is no surface peak of the Ti ions in the spectra. When samples were annealed with high temperature furnace annealing at 1400°C for one hour, they showed better damage recovery and the Ti ions diffused to the surface showing a surface peak in the RBS spectra at a channel number of 685 which corresponds to an energy value of Ti atoms on the surface of a sample. The HTF annealed spectra of a sample implanted with 10^{16} Ti/cm^2 are shown in Fig. 5.21. The

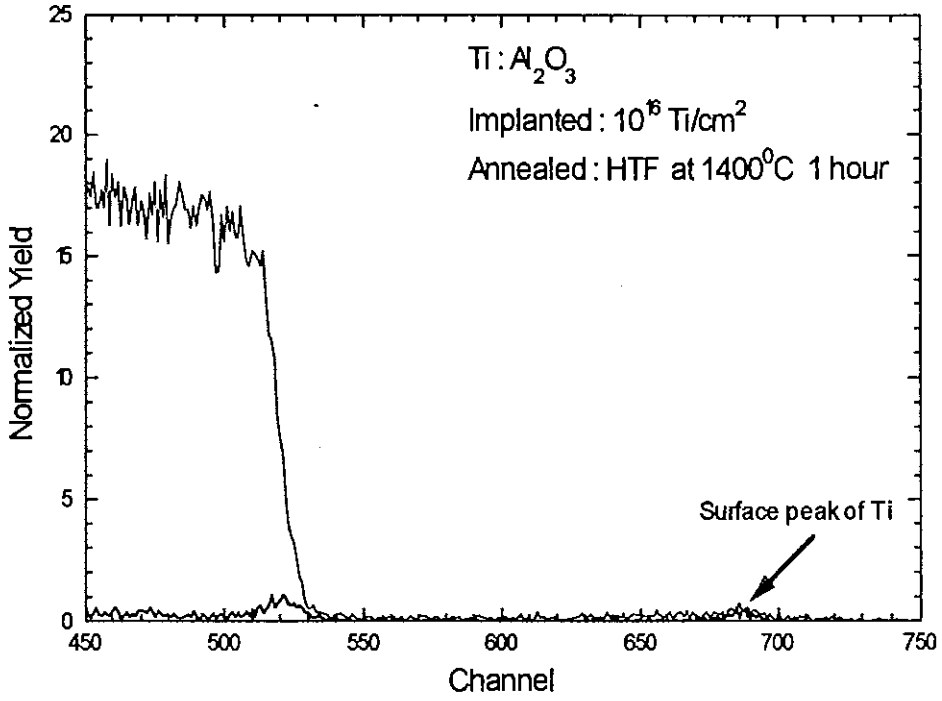

Fig. 5.21 RBS and channelling spectra of a sample implanted with 10^{16} Ti/cm^2 and annealed in the HTF at 1400^{0}C for 1 hour

spectra are drawn from channel number 450 to channel number 750 and up to a normalized yield of only 25 in order to see clearly the surface peak of the Ti atoms. In Fig. 520 the as-implanted distribution of the Ti ions were around the surface peak of the Al atoms, i.e. from channel number 450 to channel number 600, however, after the HTF annealing the Ti ions diffused up to the surface showing a surface peak of the Ti atoms in Fig. 5.21.

For comparison the RBS and channeling spectra of samples implanted with $5x10^{16}$ Ti/cm^2 and annealed in the RTA for 4x30 seconds at 1150^{0}C and in the HTF for 1 hour at 1400^{0}C is shown in Fig. 5.22. The spectra a and b are the as- implanted random and channeling spectra of a sample respectively, spectrum c is the channeling spectrum of a sample after RTA annealing for 4x 30 seconds at 1150^{0}C, and spectrum d is the channeling spectrum of another sample which is implanted with the same dose and annealed in the HTF for one hour at 1400^{0}C. In order to show the Ti concentration on the surface more clearly, the random spectra of RTA (e) and HTF (f) annealed samples are drawn in Fig 5.23

the surface, i.e. no titanium surface peak is observed in the spectrum. This is due to the fact that Ti is not mobile in sapphire at a temperature of 1150°C. However, the random (f) and channeling (d) spectra of the HTF annealed sample clearly shows the Ti ions on the surface of the sample which indicates higher mobility of the Ti ions in sapphire at a temperature of 1400°C.

To have a feeling about the substitutionality of the Ti ions in sapphire after the HTF annealing, the random and channeling spectra of a sample implanted with high dose (10^{17} Ti/cm^2) are shown in Fig. 5.24 with three values of minimum yields. The 5% minimum yield

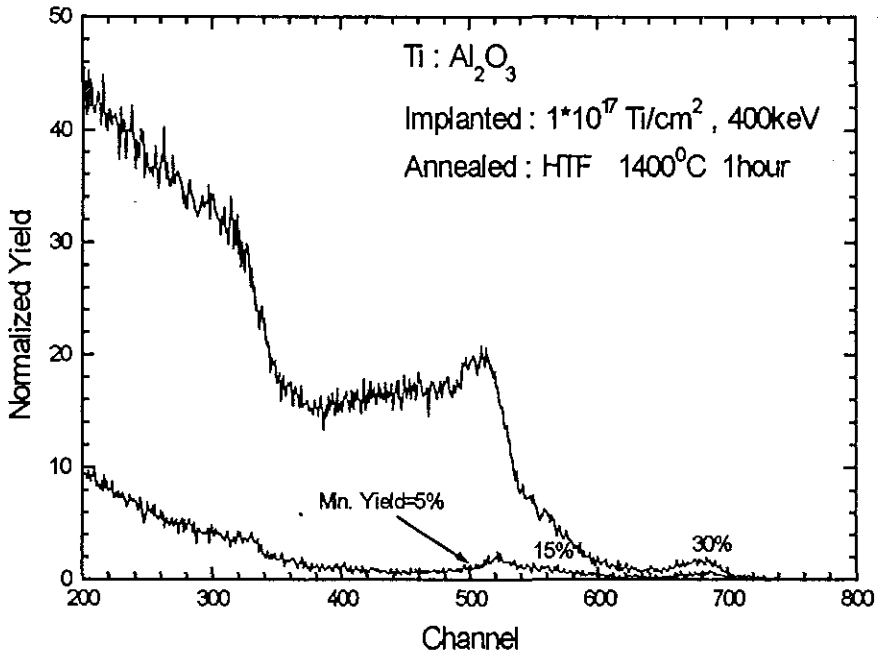

Fig. 5.24 RBS and channelling spectra of a high dose implanted and annealed sapphire

is around the surface peak of Al and is comparable with that of unimplanted crystals of Al_2O_3. Hence, almost all Ti ions in this region are incorporated into lattice sites. The next value of 15%, that is beyond the surface peak of Al, indicates that above 85% of the Ti ions are substitutional (the yields beyond the surface peak of the Al atoms (~ channel 522) are only from the Ti atoms). The 30% is from the Ti atoms on the surface of the sample estimating that at the surface, above 70% of the Ti ions are incorporated into lattice sites.

located again at the surface (like that of the 1 x 10^{16} Ti/cm^2 dose) but for 1 x 10^{17} Ti/cm^2, the peak concentration is located at the surface. This is due to the difference in the implantation doses for the same value of implantation energy. As the implantation dose increases, the damage over the implanted region increases too, which favors higher diffusion of the implanted species. Moreover, the higher the concentration of the dopants in a sample, for the same depth, the higher will be the diffusion. But if one makes the necessary combination of implantation dose and energy, it is quite possible to get a buried Ti profile after annealing in the RTA for one minute at 1060^{0}C.

RTA annealing restores crystallinity of Ti implanted $LiNbO_3$ for doses up to 1 x 10^{17} Ti/cm^2 and the samples contain narrower Ti profile than that of the implanted and oven annealed samples. The profile of the RTA annealed samples contain more Ti ions/cm than those of the oven annealed ones.

Sapphire maintains its crystallinity after implantation for doses up to 1 x 10^{17} Ti/cm^2. The microstructure of the near surface is characterized by a tangled array of dislocations extending from the surface up to a depth of the deepest implanted ions. Annealing of Al_2O_3 in oven or RTA at a temperature of 1060^{0}C does not change the RBS and channeling spectra from that of the as-implanted ones. But RTA annealing at 1150^{0}C for 4 x 30 sec., lowers the channeling spectrum significantly showing tendency of recovery of the tangled array of dislocations. However, the Ti ions do not diffuse to the surface at this temperature. While annealing of Ti implanted Al_2O_3 at 1400^{0}C for one hour lowers the channeling spectra even more significantly, and the Ti ions diffuse to the surface, showing a surface peak of Ti in the random and channeling spectra, and also most of the Ti ions are incorporated into registry of the lattice.

[17] T. Bremer, W. Heiland, Ch. Buchal, R. Irmsher and B. Stritzker
J. Appl. Phys. 67(3), (1990) 1183-1187

[18] Ch. Buchal, Nuclear Instruments and Methods in Physics Research,
B 59/60 (1991) 1142-1146, North Holland.

[19] Ch. Buchal, Nuclear Instruments and Methods in Physics Research,
B 68 (1992) 355-360, North Holland

[20] E. Glavas, J.M. Cabrera, and P.D. Townsend,
J. Phys. D Appl. Phys. 22(1989) 611-616.

[21] B.R.. Appleton, G.M. Beardsley, G.C. Farlow, W.H. Christe, P.R. Ashley
J. Mater. Res. 1(1), (1986) 104-113

[22] M. Fleuster, and Ch. Buchal, unpublished.

[23] D.B. Poker and D.K. Thomas, J. Mater. Res.,
Vol. 4, No.2, (1989) 412-416

[24] K.F. Wall and A. Sanchez, The Lincoln Laboratory Journal,
Vol 3, No. 3, (1990) 447-462

[25] D. Gelldrich, and Ch. Buchal, unpublished.

[26] C.W. White, C.J. McHargue, P.S. Sklad, L.A. Boatner, and G.C. Farlow
Materials Science Reports 4 (1989) 41-146, North Holand, Amsterdam